Received: 31 March 2024 | Revised: 4 July 2024 | Accepted: 18 August 2024

DOI: 10.1111/bre.12900

Basin Research IAS EAGE WILEY

RESEARCH ARTICLE

Kinematics of rift linkage between the Eastern and Ethiopian rifts in the Turkana Depression, Africa

Garrett Sullivan[1] | C. J. Ebinger[1] | M. Musila[1] | Mason Perry[2] | E. R. Kraus[1] | Ian Bastow[3] | Becks Bendick[4]

[1]Department of Earth and Environmental Sciences, Tulane University, New Orleans, Louisiana, USA

[2]Earth Observatory of Singapore, Nanyang Technical University, Singapore

[3]Department of Earth Science and Engineering, Imperial College, London, UK

[4]University of Montana, Missoula, Montana, USA

Correspondence
C. J. Ebinger, Department of Earth and Environmental Sciences, Tulane University, New Orleans, LA 70118, USA.
Email: cebinger@tulane.edu

Funding information
National Science Foundation, Grant/Award Number: 1824199, 1824417 and 1551823; Natural Environment Research Council, Grant/Award Number: NE/S014136/1

Abstract

Rift initiation within cold, thick, strong lithosphere and the evolving linkage to form a contiguous plate boundary remains debated in part owing to the lack of time–space constraints on kinematics of basement-involved faults. Different rift sectors initiate diachronously and may eventually link to produce a jigsaw spatial pattern, as in the East African rift, and along the Atlantic Ocean margins. The space–time distribution of earthquakes illuminates the geometry and kinematics of fault zones within the crystalline crust, as well as areas with pressurized magma bodies. We use seismicity and Global Navigation System Satellites (GNSS) data from the Turkana Rift Array Investigating Lithospheric Structure (TRAILS) project in East Africa and a new digital compilation of faults and eruptive centres to evaluate models for the kinematic linkage of two initially separate rift sectors: the Main Ethiopian Rift (MER) and the Eastern rift (ER). The ca. 300 km wide zone of linkage includes failed basins and linkage zones; seismicity outlines active structures. Models of GNSS data indicate that the ca. 250 km-wide zone of seismically active en echelon basins north of the Turkana Depression is a zone, or block, of distributed strain with small counterclockwise rotation that serves to connect the Main Ethiopian and Eastern rifts. Its western boundary is poorly defined owing to data gaps in South Sudan. Strain across the northern and southern boundaries of this block, and an ca. 50 km-wide kink in the southern Turkana rift is accommodated by en echelon normal faults linked by short strike-slip faults in crystalline basement, and relay ramps at the surface. Short segments of obliquely oriented basement structures facilitate across-rift linkage of faults, but basement shear zones and Mesozoic rift faults are not actively straining. This configuration has existed for at least 2–5 My without the development of localized shear zones or transform faults, documenting the importance of distributed deformation in continental rift tectonics.

KEYWORDS
continental rifting, fault linkage, seismicity, strain localization

1 | INTRODUCTION

For at least the past 3 Ga, Earth's continental plates have stretched and thinned in rift zones; some rupture to become new ocean basins that later close in subduction (e.g., Wilson, 1966). Yet, the dynamics of rift initiation and along-axis linkage within cold and heterogeneous lithosphere to form a contiguous plate boundary, as in the Red Sea and the East African rift system, remain debated. Hypotheses for the time–space pattern of strain localization during the early stages of rifting of cold continental lithosphere include one or a combination of lateral heterogeneities in crust and mantle composition, strength, and thickness, plate stretching forces, and the availability of magma (e.g., Burov & Diament, 1995; Buck, 2004). Heterogeneities in plate strength may localize strain (e.g., Neves et al., 2021; Petit et al., 2008). Topographic relief at the lithosphere–asthenosphere boundary may localize magma production (e.g., Koptev et al., 2018; Muirhead et al., 2020), and local heating by magma intrusion, or rapid stressing by dike and sill intrusion both localize strain (e.g., Bialas et al., 2010; Kounoudis et al., 2021; Musila et al., 2023). Favourably oriented basement shear zones may also be weak zones reactivated during rifting (e.g., Kolawole et al., 2021; Williams et al., 2022). Obliquity of pre-existing weak zones and changes in extension direction may influence rift linkage (e.g., Brune et al., 2018; Corti et al., 2019; van Wijk et al., 2017). Throughout rift evolution, the influence of one or more of these processes may lead to strain localization in spatially separated regions, requiring new structures to form and link the originally spatially separated zones of extension to form a contiguous plate boundary. These time space patterns may cause block rotations about vertical axes or lead to microplate formation (e.g., Stamps et al., 2008).

Active and ancient continental rift zones are inherently three-dimensional owing to the finite length of faults and magma intrusion processes. Rift zones show an along-axis fault segmentation into typically half-graben basins bounded on one or both sides by large offset border faults (e.g., Hayward & Ebinger, 1996; Morley et al., 1992); this fault segmentation may be replaced with a magmatic segmentation as rifting reaches seafloor spreading (e.g., Ebinger & Casey, 2001; Keranen et al., 2004). Normal faults link and grow to a length ca. 3 times the integrated elastic thickness of the plate (e.g., Cowie et al., 2000) and over time scales of 10,000–100,000 years (Kinabo et al., 2007). The border fault has the largest dimension in the fault population, and it is flanked by flexural uplifts that may rise more than 2 km above the surrounding regional elevations (e.g., Weissel & Karner, 1989). Initially discrete border fault segments interact and are mechanically connected through relay ramps and, less frequently, transfer faults oriented obliquely to the strikes of border faults (e.g., Fossen & Rotevatn, 2016; Gupta et al., 1998).

Highlights

- At rift kinks, short oblique-slip faults link arrays of normal faults aligned perpendicular to extension direction.
- Small rotations about vertical axes across the linkage zones improve fits to geodetic and seismicity data.
- Lithospheric-scale heterogeneities may have deflected rifting, but Proterozoic and Mesozoic structures are inactive.

Earthquake data from rift zones provide critical insights into basement-involved faulting patterns achieving rift zone linkage. Earthquake source mechanisms and geodetic data constrain the kinematics of border, intrabasinal, and linkage faults, enabling comparison with basement fabrics, shear zones, and compositional variations (e.g., Knappe et al., 2019; Lavayssière et al., 2019; Musila et al., 2023; Zheng et al., 2020). Earthquakes initiate in the crystalline crust beneath sedimentary basins and rupture upwards, sometimes distributing strain along multiple faults near the surface or at the basement-sedimentary contact where rock strength is at least an order of magnitude lower than the crystalline basement (e.g., Cinti et al., 2011; Zheng et al., 2020). The distribution of smaller magnitude microseisms, and potentially damaging earthquakes and their aftershocks illuminate the geometries of fault zones within the crust, as well as areas with pressurized magma bodies (e.g., Nakai et al., 2017; Oliva et al., 2019; Reiss et al., 2021). Earthquake magnitude scales with fault length; the moment magnitude of earthquakes (Mw) is proportional to fault rupture area and displacement.

Oil and gas exploration in rift basins has produced high spatial resolution images of extensional fault arrays and magmatic systems within sedimentary strata (e.g., Schofield et al., 2021). Yet, the geometry and kinematics of basement-involved fault arrays and their relationship to crust and mantle thinning and magma intrusion remain poorly understood (e.g., Brune et al., 2023; Olive et al., 2022). Multi-physics models rarely consider the role of strain accommodation by magma intrusion and local heating (e.g., Bialas et al., 2010), or of the role of short duration, intense faulting and/or magma intrusion events as opposed to time-averaged strains (e.g., Ebinger et al., 2023; Oliva et al., 2019). Our approach is to use local seismicity and geodetic data to characterize basement-involved fault kinematics and extension accommodated by magmatism

over short time scales using data from the zone of linkage between two rift zones separated by ca. 300 km: the southern Main Ethiopian rift (MER) and the northern Eastern rift (ER) through the Turkana Depression (Figure 1). The region has significant pre-rift lithospheric-scale heterogeneities; Cenozoic structures cross-cut Mesozoic rifts and parts of the Eo-Oligocene Ethiopia-Yemen flood basalt province (e.g., Ogden et al., 2023; Steiner et al., 2022) which is underlain by heterogeneous mantle lithosphere associated with the oceanic terranes accreted during the Pan-African orogeny (Kounoudis et al., 2021, 2023).

In large part owing to data gaps, a variety of models have been proposed for the low-elevation region between the Ethiopian and E African plateaus. Existing numerical and analogue models for rift linkage in this area involve a pre-existing weak zone between two propagating rifts and assume synchronous development across a very broad zone (Brune et al., 2017; Corti et al., 2019); diffuse NE to ENE-striking transcurrent fault(s) that reactivate(s) basement structures (e.g., Brune et al., 2018; Vétel & Le Gall, 2006); reactivation of the NW-striking Proterozoic Aswa shear zone as a continental transform (Chorowicz, 2005; Katumwehe et al., 2016). This area, therefore, affords an opportunity to understand the kinematics of fault linkage during rift migration and propagation within a magmatic rift zone.

Our study uses seismicity and geodetic data from the Turkana Rift Array Investigating Lithospheric Structure (TRAILS) project and a new digital compilation of Cretaceous-Recent faults (Supplementary Material), and Oligocene-Recent eruptive centres to evaluate (1) the geometry and kinematics of active border and transfer faults linking extensional basins and (2) models for the kinematic linkage of two initially separate rift sectors through

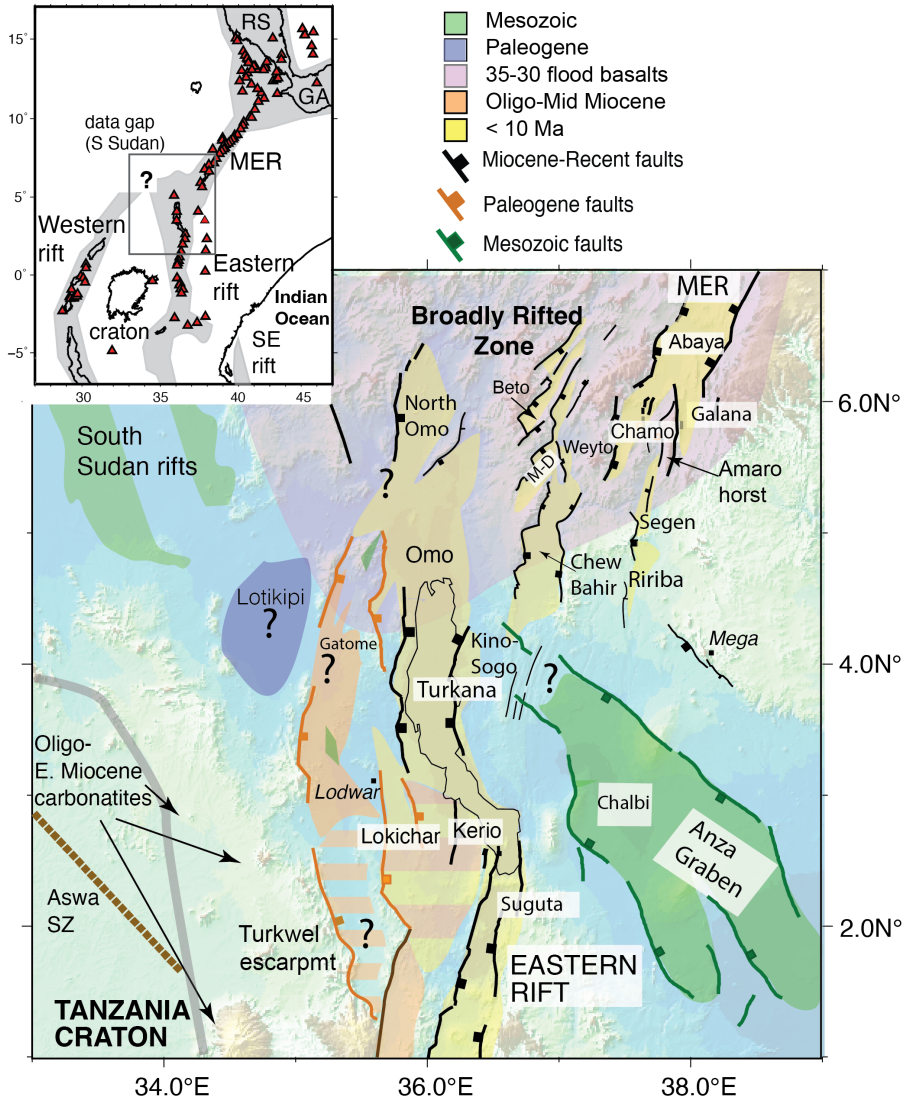

FIGURE 1 Mesozoic, Palaeogene, and Oligocene-Recent rift basins overlain on topographic relief after Bosworth and Morley (1994); Ebinger et al. (2000); Tiercelin et al. (2012); Philippon et al. (2014); Torres Acosta et al. (2015). Inset: Main Ethiopian rift (MER), Eastern rift, and Western rift with Holocene volcanoes (red triangles).

a ca. 300 km-wide broadly rifted zone (BRZ) whose breadth is a consequence of a lateral migration of rifting, as well as extension of heterogeneous lithosphere, as outlined below. Musila et al. (2023) present the new seismicity data set and establishes a regional context for our study of basin linkage between two initially widely separated, migrating rift zones.

2 | TECTONIC AND GEODYNAMIC SETTING

The African plate overlies one or more low-velocity zones that rise from the core–mantle boundary to the base of the African plate (e.g., Boyce et al., 2023; Chang et al., 2020); the upwellings drive uplift, extension and magmatism (e.g., Koptev et al., 2018; Muirhead et al., 2020) (Figure 1). Although the Turkana Depression between the Ethiopian and East African plateau had been interpreted as evidence for two separate mantle upwellings, the region has experienced 400–500 m of uplift since Miocene time (e.g., Wichura et al., 2015), consistent with isostatic models of crustal thickness variations (Ogden et al., 2023). The low-elevation area between the Ethiopian and East African plateaus, therefore, is largely a consequence of the Mesozoic crustal thinning, and the entire region is dynamically supported (Boyce et al., 2023; Kounoudis et al., 2021; Ogden et al., 2023).

The MER and the ER sectors formed in Proterozoic lithosphere east of the thick (>150 km) Archaean Tanzania craton. NNW to N-S-striking Neoproterozoic island-arcs and microcontinents accreted east and north of the craton during the Pan-African orogen (800–550 Ma) (e.g., Abdelsalam & Stern, 1996; Fritz et al., 2013; Figure 2). Northeastern Africa was rifted subsequently in Cretaceous (130–80 Ma); Palaeogene (ca. 60–50 Ma); and Oligo-Miocene to Recent times (ca. 27–0; e.g., Ebinger et al., 2000; Morley et al., 1992; Philippon et al., 2014; Tiercelin et al., 2012; Figures 1 and 3). The Cretaceous rifting episode created the NW-SE trending Anza Graben and the South Sudan rifts (e.g., Bosworth & Morley, 1994) that contain sedimentary and volcanic strata (Winn et al., 1993; Figure 1). Palaeogene rifting and uplift along the northeastern Tanzania craton margin (Owusu-Agyemang et al., 2019; Torres Acosta et al., 2015) and in what is now the southern MER (Erbello et al., 2024) is inferred from thermochronological data and stratal ties to seismic reflectors beneath the Lotikipi basin (Hendrie et al., 1994; Tiercelin et al., 2012), but there is no evidence for extensional faulting beneath the oldest (ca. 45 Ma) lavas of the Ethiopian flood basalt province north and northeast of the Turkana Depression (Davidson & Rex, 1980; Ebinger et al., 2000; Erbello et al., 2022; Figure 1).

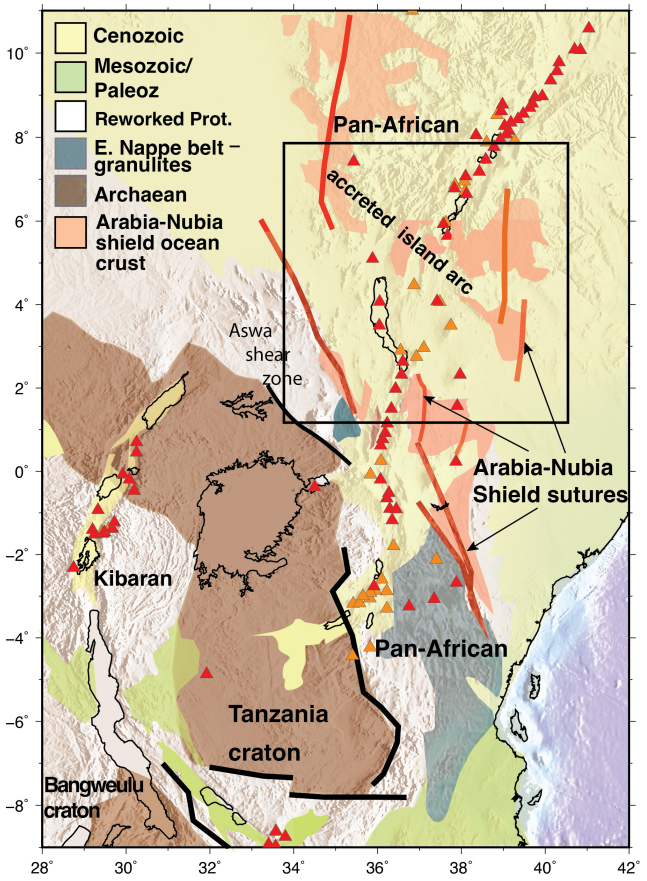

FIGURE 2 Tectonic domains after Fritz et al. (2013) and Boniface and Appel (2018). Archaean cratons have unusually thick lithosphere (>150 km), compared to 100–120 km-thick Proterozoic orogenic belts, and ≤100 km-thick Mesozoic passive margins (e.g., Fishwick & Bastow, 2011). Black lines are Proterozoic sutures; red lines are Pan-African sutures; orange line indicates Pan-African reactivation; orange triangles: Pleistocene volcanic centres. Red triangles: Holocene eruptive centres from Global Volcanism Program (2023).

We summarize the diachronous magmatic and faulting history to establish time–space context for the current linkage of the MER and ER, and its relationship to pre-existing heterogeneities. Widespread and voluminous magmatism with no stratal tilting occurred in southwestern Ethiopia at ca. 47–35 Ma prior to rapid outpourings 32–30 Ma along the Red Sea, and along the future site of the Turkana rift (e.g., Ayalew et al., 2021; Davidson & Rex, 1980; Ebinger et al., 2000; Morley et al., 1992). Formation of sedimentary basins in the Turkana region initiated at ca. 28 Ma soon after magmatism (Erbello et al., 2024; Morley et al., 1992; Ragon et al., 2019). Between 27 Ma and Recent time, magmatism and faulting migrated eastwards from near the Archean Tanzania craton edge to the region east of Lake Turkana (Brune et al., 2017; Franceschini et al., 2020; Key et al., 1987; Shinjo et al., 2011). Faulting in the southern MER initiated considerably later at about 15–20 Ma

based on dating of eruptive centres along border faults (Ebinger et al., 2000; Franceschini et al., 2020; McDougall & Brown, 2009; WoldeGabriel et al., 1990), and time–temperature reconstructions from basement exhumation ages (Balestrieri et al., 2016; Boone, Balestrieri, et al., 2019; Philippon et al., 2014). Erbello et al. (2024) find a period of rapid basement cooling at ca. 27 Ma along the flanks of the Mali-Dancha basin north of the Chew Bahir basin, suggesting that faulting in at least one part of the BRZ initiated synchronously with the Turkana region.

Holocene and historic magmatism continues at Kuraz (Korath) volcano north of Lake Turkana, at North, Central, and South Island volcanoes that emerge from Lake Turkana, Kulal volcano and the central rift valley volcanoes of the Suguta rift, the northernmost sector of the ER zone (Figures 2 and 3). Largely unfaulted Holocene eruptive centres east of the zones of active faulting include Marsabit and Hurri Hills shield volcanoes and the Dilo (Dukana) and Mega monogenetic cone complexes; these eruptive centres lie above an upper mantle low-velocity zone at depths of 300–500 km (Kounoudis et al., 2021; Figures 2 and 3). Shield construction east of Lake Turkana diverted Omo river drainage to the Indian Ocean along the Anza rift in Pliocene time, and reshaped Lake Turkana (Bruhn et al., 2011).

The kinematics of rifting between the MER and ER and the Western rift has long been debated, in large part owing to the limited crustal imaging and fault kinematics data. The few teleseismically detected earthquakes that have occurred in the region (M > 4) show oblique and normal slip (Figure 3), but these earthquakes have location uncertainties of 25 km or more and cannot be linked to specific structures (e.g., Musila et al., 2023; Weinstein et al., 2017; Figure 3). GNSS data indicate 5–7 mm year^{-1} of N95°E ± 10° opening in the MER north of our study area (Birhanu et al., 2016). Philippon et al. (2014) estimated a N105°E extension direction in the MER and N135°E in the BRZ using surface fault slip indicators, and they suggested some counterclockwise rotations around vertical axes. Musila et al. (2023) determine an extension direction of N140° + 18°/−28° E across the BRZ from inversion of earthquake focal mechanism solutions. GNSS data show spatial variations ranging from N65°E southwest of the MER to N140°E in the BRZ that suggests rotations about vertical axes (Figures 3 and 4). Across the Turkana Depression, extension direction from Kostrov summation of teleseisms and inversion of local earthquakes is N88°E + 18°/−25° for the Turkana rift region (Musila et al., 2023). Campaign and continuous GNSS data record an average of ca. 4.7 mm year^{-1} ca. E-W extension relative to stable Nubia, with localization to the <100 km-wide Lake Turkana basin (Knappe et al., 2019; Musila et al., 2023).

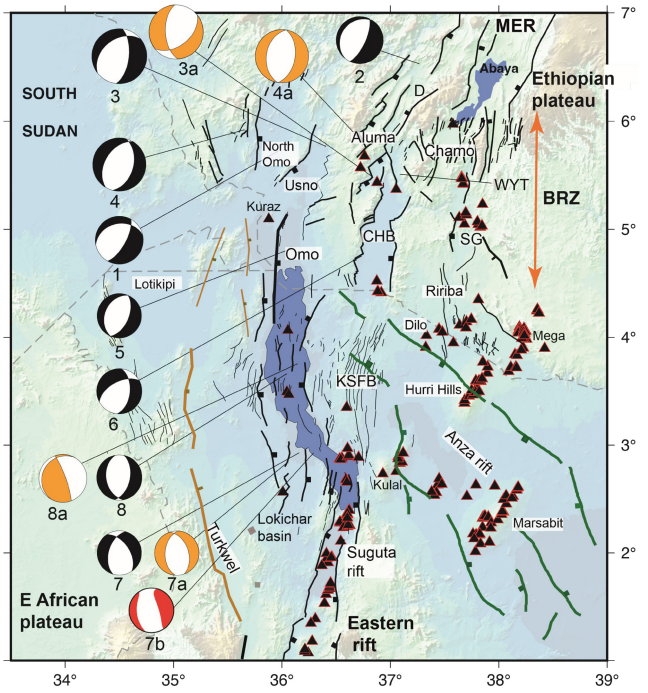

FIGURE 3 Source mechanisms of teleseismically detected earthquakes from the Global Centroid Moment Tensor (gCMT) catalogue between 1983 and 2023 (Dziewonski et al., 1981; Ekström et al., 2012)(Table S1) across the Broadly Rifted Zone (BRZ) and Turkana Depression. Red is the full moment tensor source solution for the 2020-03-05 Mw 5 (4.5 M_L) Event 7b (Musila et al., 2023). Orange CMT is the solution from teleseismic arrivals labelled as 7a (Craig & Jackson, 2021). FMT solutions computed for pre-2019 teleseismically detected earthquakes in the region include Events 3a and 4a by Foster and Jackson (1998) and Event 8a (Craig & Jackson, 2021) in orange. Event location errors may be as large as 50 km (compare 4 and 4a locations); the gCMT location for the May 3rd, 2020, event (Event 7) differed by 11 km from our precise location (Musila et al., 2023). Mesozoic-Palaeogene and Cenozoic fault structures in purple and black, respectively, and Quaternary-Recent eruptive centres in black triangles. Lake Turkana shaded in blue. MER, D, WYT, CHB, SG, KSFB are the Main Ethiopian Rift, Dancha, Weyto, Chew Bahir, Segen, Kino Sogo Fault Belt, respectively.

The along-axis propagation and eastward migration of faulting and magmatism sequence outlined above does not support the propagating overlapping rift model of Brune et al. (2017) that predicts synchronous and broadly distributed Cenozoic strain across the Mesozoic rift zone, which was assumed to be a weak zone. The thinner crust (ca. 27 km) beneath the Cretaceous Anza rift, therefore, means that lithosphere has a larger percentage of strong mantle than the surrounding regions with ca. 40 km-thick crust; this area may have been stronger than surrounding areas with thicker crust (Ogden et al., 2023). Chorowicz (2005) and Katumwehe et al. (2016) propose that the NW-striking Proterozoic Aswa shear zone was re-activated as a left-lateral transform fault linking the Western and ERs, but

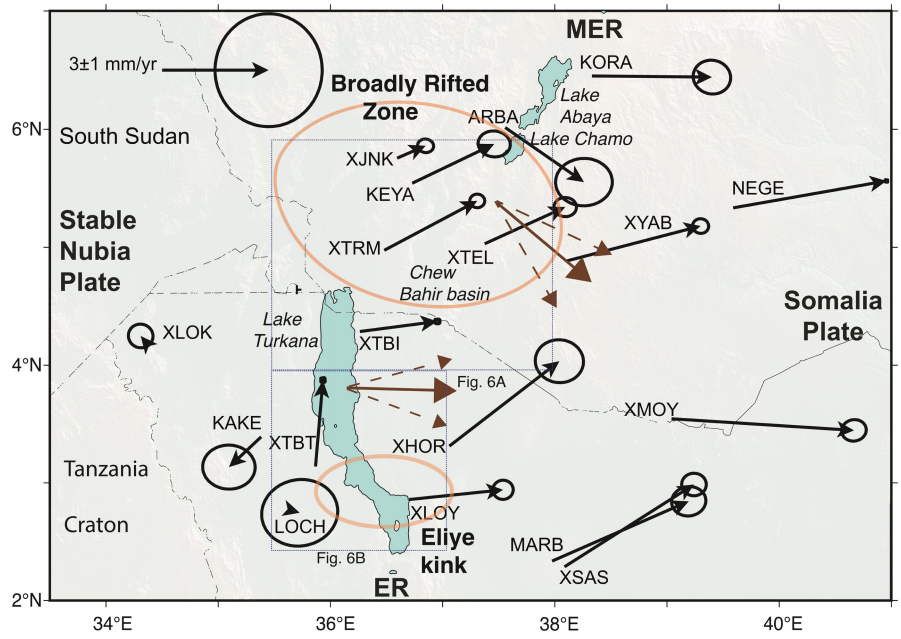

FIGURE 4 GNSS opening velocities with 2 sigma uncertainties of Somalia plate relative to stable Nubia with caveat that Nubia-Somalia boundary in northwestern part of the region is poorly determined owing to data gaps in South Sudan. Brown arrows indicate opening direction from Kostrov summation of teleseismic earthquakes and from inversion of local earthquake source mechanisms, with 2 sigma uncertainties (from Musila et al., 2023). Grey ellipses outline major kinks in the orientation of the rift zone—the focus of this study. ER, Eastern rift; MER, Main Ethiopian rift. See also Pliocene-Recent slip indicators from Philippon et al. (2014) in Figure 5.

geodetic and seismic data show no evidence for seismicity or aseismic slip along the Aswa fault zone and instead show approximately E–W extension, not NW-SE extension (Knappe et al., 2019; Musila et al., 2023). These earlier regional studies, however, did not evaluate the kinematics of border faults, inter- and intra-basinal fault linkage, the focus of this study.

3 | DATA AND ANALYSES

3.1 | Seismicity

We use subsets of the TRAILS seismicity catalogue (2019–2021) relocated using waveform cross correlation of P-wave first arrivals and a double-difference algorithm with location uncertainties <0.9 km and ≤1.5 km in depth, and with local magnitude $1 \leq M_L \leq 4.5$ (Musila et al., 2023) to interpret the kinematics of border fault and rift segment linkage. Earthquake locations along three representative cross sections as well as existing constraints on crustal thickness, sedimentary basin geometry, and stratal ages reveal active faulting and their relation to Quaternary eruptive centres. The ca. 2-year time span of seismic observations and ≤7 years for GNSS data for the TRAILS array is much shorter than the earthquake cycle for potentially damaging tectonic earthquakes. Teleseismically detected earthquakes (Mw >4) from 1985 to present provide additional constraints on rift kinematics (Figure 3) but location uncertainties of 11–24 km mean these earthquakes cannot be associated with a specific fault system without corresponding field evidence (e.g., Musila et al., 2023; Weinstein et al., 2017).

3.2 | Earthquake source mechanisms

Source mechanism solutions are published in Musila et al. (2023) and in Table S1 (Figure 6).

3.3 | Stress inversion

We complement the estimates of extension direction across the BRZ and Turkana Depression in Musila et al. (2023) with new estimates of principal stress directions in the eastward step in the Turkana rift, referred to as the Eliye kink that includes 15 earthquake source mechanisms (ellipse in Figure 5). We use the bootstrap resampling program MSATSI (Martinez Garzon et al., 2014).

3.4 | GNSS data

Twelve continuous and 8 campaign GNSS stations throughout Ethiopia and Kenya as well as continuous

stations from the International GNSS service (IGS) that give a standard global reference frame (Knappe et al., 2019; Musila et al., 2023) were used to evaluate plate kinematic models (Figure 4).

3.5 | Synthesis of structures and eruptive centres

Field mapping prior to the availability of satellite locations relied on air photos and 1:250,000 topographic maps (e.g., Davidson & Shiferaw, 1983; Ebinger et al., 1993, 2000; Moore & Davidson, 1978; Morley et al., 1992; WoldeGabriel & Aronson, 1991). We adjust locations of faults mapped from air photos and pre-GPS seismic reflection data, and synthesize published structural interpretations in smaller parts of the study area that were validated with field studies (Alemu, 2017; Bruhn et al., 2011; Corti et al., 2019; Erbello et al., 2022; Franceschini et al., 2020; Hackman et al., 1990; Muirhead et al., 2022; Philippon et al., 2014; Ragon et al., 2019; Schofield et al., 2021; Tiercelin et al., 2012; Vétel & LeGall, 2006). Subsurface interpretations of faults from gravity, seismic reflection, and magnetotelluric data were calibrated with sparse well data (Abdelfettah et al., 2016; Hendrie et al., 1994; Muirhead et al., 2022; Schofield et al., 2021; Tiercelin et al., 2012; Winn et al., 1993). For areas with only lineament or large-scale mapping, structures of length >2 km in multiple DEMs exhibiting three or more of the following criteria were mapped as faults: lineation, triangular fault scarps, vegetation change, drainage change, asymmetric relief, and geologic non-conformities. Eruptive vents, cinder cones, ash and tuff cones, and maars were delineated by collating results of previous mapping projects (Davidson & Shiferaw, 1983; Ebinger et al., 2000; Franceschini et al., 2020; Hackman et al., 1990; Morley, 2020) using the morphology criteria established by Franceschini et al. (2020).

3.6 | Kinematic Modelling

As a test of different large-scale kinematics of the linkage zone between the MER and the ER, we construct a series of simple rigid block models using TDEFNODE (McCaffrey, 2009). Are spatial variations in GNSS vectors across the BRZ consistent with a slowly rotating microplate (Figure 4)? We approximate the boundaries of the blocks using the seismogenic zones, varying the geometry of linkage through the BRZ and evaluating the possible role of the Mesozoic rift structures. The motions of the blocks are defined by Euler rotation poles defined by our GNSS velocities, and interseismic slip is applied to block boundaries. TDEFNODE iterates to minimize the misfit to the observed velocity field (Figure 4). In all models, faults are input from either the GEM global fault database (Styron & Pagani, 2020) updated with our work, and including the locations of Mesozoic faults (Figure 5). Given the en echelon geometry of faults, our input faults are connected using pseudo-faults, which are essentially free slip boundaries. To test the validity of our models, we calculate the RMS error for each model from the residuals of predicted GNSS velocities. Additionally, to account for increasing the complexity of the model, we utilize the least squares case of the Akaike information criterion (AIC), and its sparse observation equivalent (the AIC_c) (Akaike, 1974; Burnham & Anderson, 2002).

4 | RESULTS

We summarize spatial patterns in faulting and seismicity to evaluate models for current rift linkage in map view and cross sections, integrating surface fault and basin geometry, sediment thickness, earthquake source mechanisms, seismicity, and Moho depth along three cross sections spanning the zone of linkage between the southern MER and the northern ER. These cross sections highlight abandoned basins and eruptive centres, along and across-rift differences in fault geometry, and their relation to magmatism, crustal thickness variations, and relationship to Mesozoic rift structures (Figures 5–7).

4.1 | Spatial distribution of Seismicity and Faulting

4.1.1 | Northern BRZ (Profile A-A′)

In the southern MER at the northern limit of our study area, seismicity and Quaternary magmatism are localized to the ca. 80 km-wide, Abaya basin (Ogden et al., 2021; Philippon et al., 2014; Figure 5). Seismic reflection imaging indicates up to 3600 m of sedimentary strata in the westward-tilted half-graben (Kebede et al., 2023). Source mechanisms of four local earthquakes along the western border fault show normal slip along N–S to N30°E striking nodal planes (Ogden et al., 2021). Fault slip data in Pliocene-Recent strata indicate WNW-ESE directed extension (Philippon et al., 2014) (blue arrows, Figure 5), consistent with GNSS data (Birhanu et al., 2016).

Moving southwards, the seismically active zone broadens to nearly 300 km across the BRZ, an area underlain by fast wavespeed lithosphere corresponding to a NW-trending mafic-ultramafic accreted terrane (Kounoudis et al., 2021). The BRZ comprises many

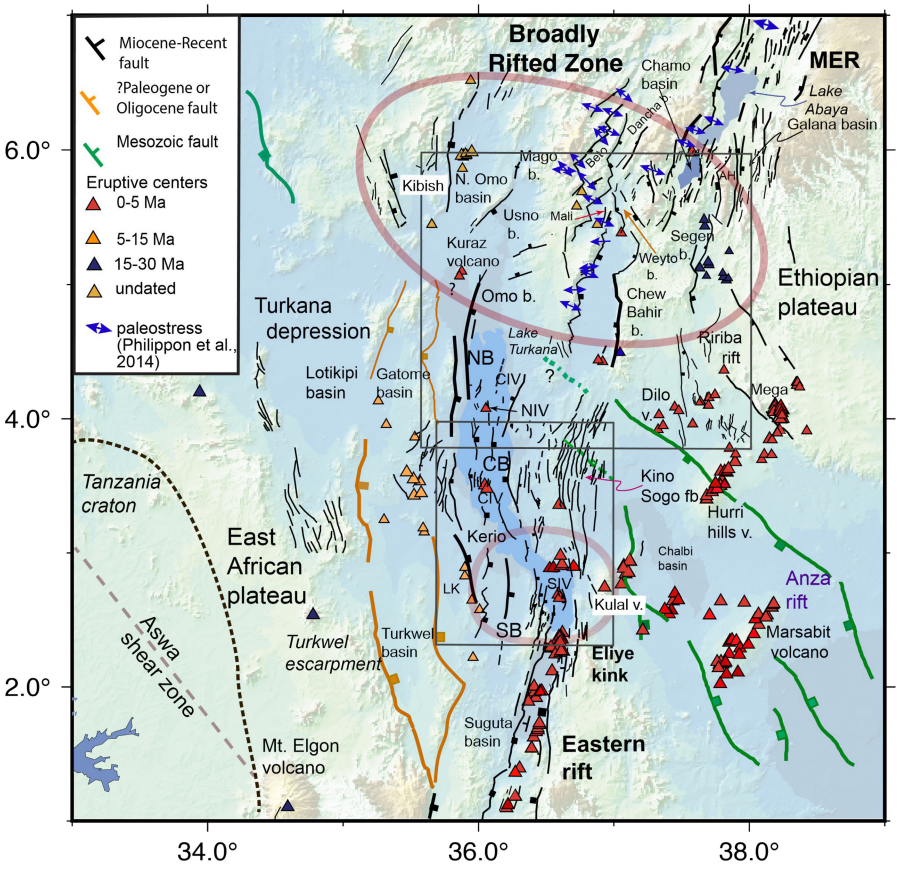

FIGURE 5 Structures and Eocene-Recent eruptive centres, where known. Faults were collated from Davidson (1983); Corti et al. (2019); Smith and Mosley (1993); Moore and Davidson (1978); Morley et al. (1992); Erbello et al. (2022); Ebinger et al. (1993, 2000); Philippon et al. (2014); Schofield et al. (2021); and Muirhead et al. (2022). Volcanic centres were mapped using a combination of previous works including Franceschini et al. (2020); Morley (2020); Tiercelin et al. (2012); and Davidson and Shiferaw (1983). Where age data are available, volcanic centres were grouped into a 0–5 Ma red and >5 to 38 Ma in blue; undated centres are in yellow.

sub-parallel fault-bounded basins connected by short NW-striking faults: from west-to-east: Kibish, North Omo, Mago-Usno, Beto-Mali-Dancha, Weyto (Weyito), Chamo, Segen, and Galana-Ririba basins (Davidson & Shiferaw, 1983; Ebinger et al., 2000; Erbello et al., 2022, 2024; Philippon et al., 2014; Figures 5 and 6). Primarily basaltic magmatism between 45 and 35 Ma preceded basin formation across this region but there is no evidence for stratal thickening indicative of extension (e.g., Davidson & Rex, 1983; Ebinger et al., 2000; George et al., 1998).

4.1.1.1 | *Usno-Mago basins*

The westward-tilted Usno-Mago basin is ca. 30 km wide and ca. 60 km in length, but the thickness of sediments in the basin is unconstrained. A sedimentary basin existed by 4.2 Ma when the youngest known lavas in this area were erupted from fissures along what is now the NNE-striking western border fault (Davidson & Rex, 1980), but the basin age could be considerably older.

4.1.1.2 | *Aluma (Beto), Mali-Dancha, Weyto basins*

The border faults and transfer faults linking basins comprise both NE and NNW-striking faults that parallel metamorphic fabrics in some areas (e.g., Corti, 2009; Erbello et al., 2024). Faulting and initial deposition began between 18 and 13 Ma when small alkali basalt and phonolitic eruptive centres developed near or along developing border faults (Ebinger et al., 1993; Philippon et al., 2014). Crustal thickness decreases from 30 to 35 km to ca. 26 km beneath the Weyto basin (Figure 7a). The 25 October 1987 Mw 6.1 earthquake occurred along or near the Beto basin border fault based on field studies by Asfaw (1990); the source mechanism indicates normal slip along approximately N–S striking nodal planes (3a, Figure 3). Three days later, an Mw 5.6 oblique-slip earthquake occurred in the same region, with N-S and NE-striking nodal planes (4a, Figure 3). Earthquakes span surface to 20 km depth and largely coincide with normal and oblique slip faults (Figures 5 and 6). Event 53 between the Beto and Mali basins indicates normal slip along NW-striking fault planes. Events 43 and 36 within the basin show oblique extension along NNE and NE-striking nodal planes (Figure 6).

4.1.1.3 | *Chamo, Segen basins*

The narrow Chamo basin is the southward continuation of the Abaya basin; the two basins are separated by a chain of <1.34–0.68 Ma eruptive centres (Ebinger et al., 1993). It is bounded by a border fault on the west and by the ca. 3000 m-high Amaro horst to the east. Lacustrine mudstones were deposited by Mid-Miocene time in the southern Chamo basin coeval with eruption of alkali basalts and phonolites (WoldeGabriel et al., 1991). Both sides of the Segen basin to the southeast of the Chamo basin are

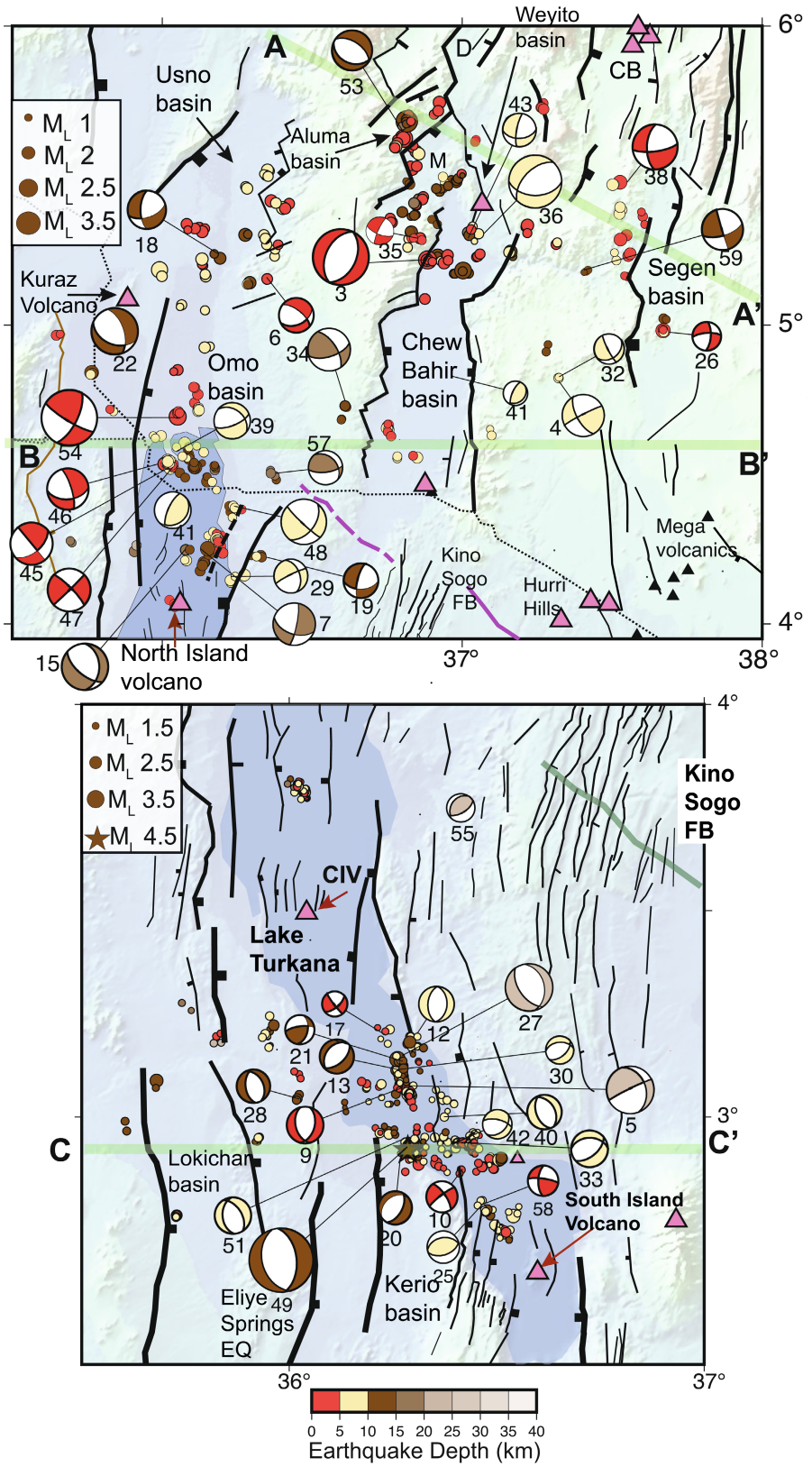

FIGURE 6 Source mechanisms of local earthquakes recorded on the TRAILS array (Table S1) colour coded by depth and scaled by magnitude across the BRZ (top) and the Eliye kink (bottom). The Mw 5.0 (M_L 4.5) Eliye Springs earthquake (Event 49, Table S2) is denoted by a star. CB, Chamo basin; CIV, Central Island Volcano; MD, Mali-Dancha basins.

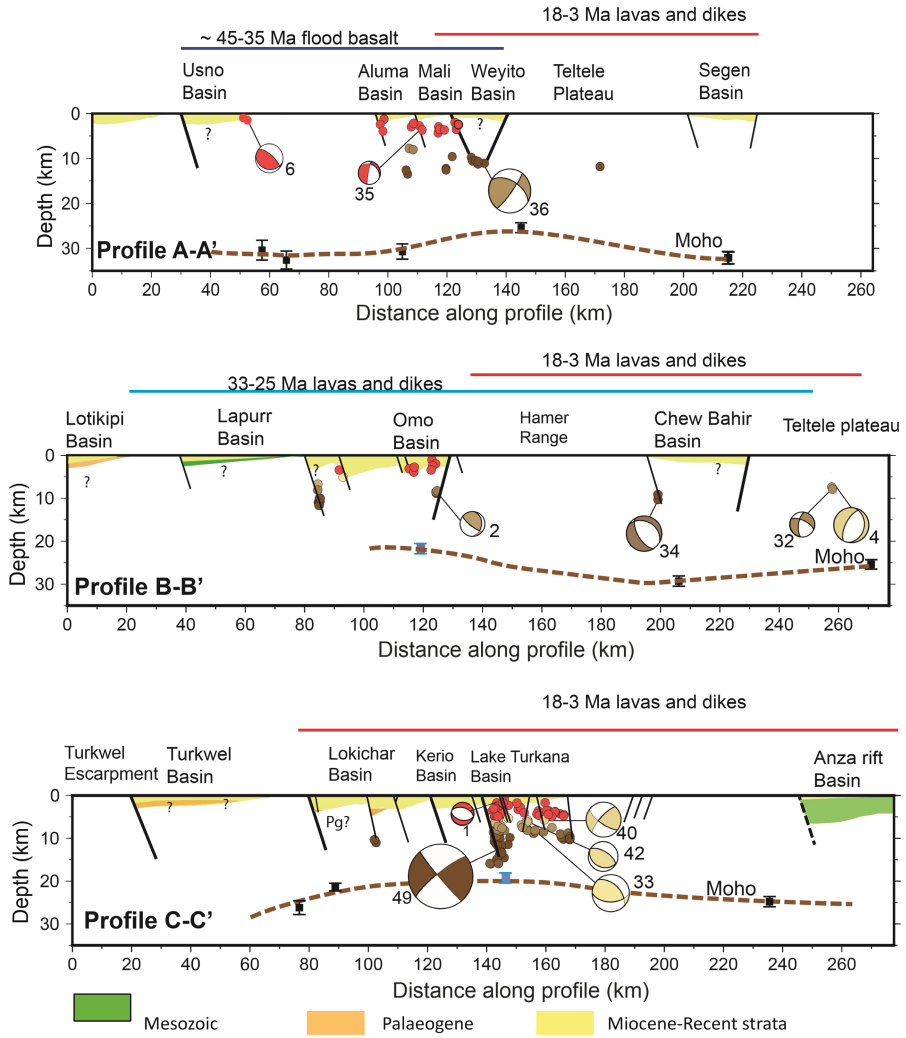

FIGURE 7 Cross sections A-A′, B-B′, and C-C′ across the broadly rifted zone (Figure 2) with relocated earthquakes and source mechanisms. Brown dashed line is an estimate of Moho depth based on crustal thickness from receiver functions shown with brown squares (Ogden et al., 2023) and from controlled source imaging with blue squares (Mechie et al., 1994). Subsurface faults from Dunkleman et al. (1989); Dindi (1994); Alemu (2017); Schofield et al. (2021); Nutz et al. (2022).

flanked by N-S striking border faults (Ebinger et al., 2000; Philippon et al., 2014). The Segen basin is characterized by a few scattered, shallow earthquakes located on or near border faults (Figures 5 and 6). The earthquake source mechanism for event 38 between the Chamo and Segen basins is left-lateral strike-slip along approximately E–W nodal planes. Earthquake 26 in the southern Segen basin has a similar source mechanism (Figure 6).

4.1.1.4 | *Weyto (Woyito) basin*

The Weyto basin is one of the most seismically active parts of the rift (Figures 5 and 6). Its northern limit is delimited by an N75°E-trending line of earthquakes at depths of 0–20 km interpreted as a transfer fault zone (Figure 6). Event 35 lies on the western flank of the Weyto basin; left lateral motion along the N100°E nodal plane is subparallel to short fault segments along the border fault. Shallow events 36 and 43 in the central basin are oblique normal along NNE-striking nodal planes, whereas event 3, a shallow M_L 3.3 earthquake along the western border fault, indicates normal slip along N20°E nodal planes. The ENE orientation of strike-slip faults is nearly orthogonal to the NW strike of the accreted terrain structures, but parallel to some undated brittle structures in metamorphic basement (Philippon et al., 2014).

4.1.2 | Southern BRZ, Profile B-B′

At ca. 5.5 N, the seismically active zone narrows to <200 km across the Omo and Chew Bahir basins; the Teltele plateau and Ririba rift to the east are largely inactive, consistent with fault morphology interpretations (Corti et al., 2019). The 45–37 Ma flood basalts pre-dating

rifting are thin to absent in this rift swath (e.g., Ebinger et al., 2000; Steiner et al., 2022). Instead, basement is overlain by localized basalts erupted between 37 and 32 Ma and sedimentary strata deposited in fault bounded basins by about 28 Ma (e.g., Davidson & Rex, 1980; Morley et al., 1992; Ragon et al., 2019).

4.1.2.1 | *Omo-N Turkana basin*

The Omo-N Turkana basin is a westward-tilted half graben with a low-relief, N-S-striking border fault system that is about 75 km long (Alemu, 2017; Dunkleman et al., 1989; Nutz et al., 2022). Cretaceous to Palaeogene sediments crop out west of northern Lake Turkana, and show NW palaeodrainage directions, suggesting that the Anza rift underlies northern Lake Turkana (Owusu-Agyemang et al., 2019; Tiercelin et al., 2012; Figure 6). Uplift and erosion of a pre-existing sedimentary basin, therefore, may explain the low relief flanks. Reflection seismic data calibrated by well data indicate ca. 2.5 km of Lower Miocene to Recent sediments in the Omo basin (Ethiopia), thickening to ca. 4 km of sedimentary and interbedded volcanic strata in the North Basin of Lake Turkana (Alemu, 2017), consistent with gravity models (Mammo, 2012). Synthetic faults define a series of westward-tilted fault blocks (Nutz et al., 2022) that are seismically active to depths of 15–20 km (Figures 6 and 7), with occasional igneous intrusions (Dunkleman et al., 1989). Two Holocene volcanoes developed within the westward tilted half-graben: the 91 ± 15 ka Kuraz (Korath) shield volcano in the west-central section of the Omo basin (Jicha & Brown, 2014) and North Island volcano (NIV), flows of which post-date 10 ka (Dunkley et al., 1993; Key & Watkins, 1988; Figure 8b).

Seismicity occurs across both the western and eastern uplifted flanks of the Omo and N. Turkana basins spanning the Ethiopia–Kenya border and at depths from surface to 20 km (Musila et al., 2023). Local and teleseismically detected earthquakes indicate extension along NNW to NNE-striking faults as well as ENE-striking transfer faults. The majority of focal mechanisms indicate oblique to strike-slip along NW- or NNE-striking nodal planes, and span 20 km subsurface. Events 22 and 15 indicate normal slip along approximately N–S to NNW striking planes, whereas event 39 indicates oblique normal slip along ENE or NW nodal planes. The largest event in the basin, M_L 3.2 (event 54), is strike-slip along sub-vertical NW or NNE-striking nodal planes. Events 7, 29, 45, 46, 47 and 48 at the northern end of Lake Turkana and its eastern flank are right lateral oblique NNE to NE-striking nodal planes. Events on the eastern side of the N Turkana-Omo basin indicate oblique normal slip along NE or NW-striking nodal planes. Both right lateral and left lateral slip are consistent with short faults achieving linkage between approximately N–S striking, sub-parallel normal faults. Event 41 in the south-central part of the North Turkana basin indicates reverse oblique slip along N15°-45° E-striking planes. Along the southeastern side of the basin, seismicity outlines a NNE-striking fault zone that terminates south of NIV (Figure 6). This fault zone may serve to link magma intrusion zones to rift bounding fault systems in a geometry similar to that of the Natron-Manyara rift zone (e.g., Oliva et al., 2019). Teleseismically detected events 1, 4, 5 with magnitudes Mw > 4, an order of magnitude larger than the local events we detect, are normal faulting events with N20-45° E striking nodal planes (Figure 3, Table S1).

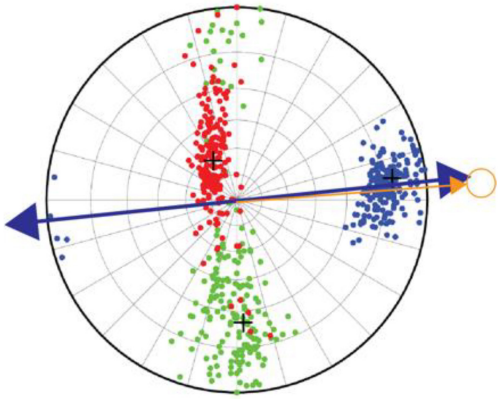

FIGURE 8 Bootstrap solutions for stress inversion of local earthquake source mechanisms within the Eliye Kink. Red circles indicate σ_1, green circles—σ_2, and blue circles—σ_3. Blue line indicates best-fitting opening direction of N82E +20/−24°; orange arrow is geodetically determined extension direction (Musila et al., 2023). The smearing of σ_2 is expected with both left lateral and right lateral slip planes in these closely spaced extensional fault arrays.

4.1.2.2 | *Chew Bahir basin*

The Chew Bahir basin is bounded by steep border faults on both its western and eastern sides, and its eastern flank rises more than 1000 m above surrounding topography. The northern Chew Bahir is linked to the Weyto basin by a well-developed step-over characterized by transfer faults in a broken relay ramp, the largest of which is ca. 15 km long (Figures 5 and 6). The earliest sedimentary strata are not known in the Chew Bahir basin, but trachytic centres displaced by the eastern Chew Bahir border fault indicate initial faulting by about 19 Ma. Depth to basement is estimated at 2.5 km from models of gravity data (Ebinger et al., 2000). There are no intra-basinal faults seen at the surface owing to high sedimentation rates (0.47 mm year^{-1}; Roberts et al., 2021).

Seismicity is concentrated along border faults that include short (≤10 km) NW-striking faults that parallel the strong metamorphic fabric of the NW-trending ultramafic belt, where exposed beneath 45–0 Ma lavas (Figure 1,

structure). A Mw 5.1 earthquake in 2011 (event 6) occurred within or near the Chew Bahir basin (Figure 3, Table S2). Seismic activity is concentrated along a subsurface projection of the western border fault. Event 34, a left-lateral oblique reverse fault occurred at a depth of 17.4 km along the horst between the Chew Bahir and Omo basins (Figure 6).

4.1.2.3 | *Ririba rift*

At ca. 4° N, a system of N-S striking faults cutting ca. 3.7 Ma lava flows is termed the Ririba rift, separated from the Chew Bahir basin by the Teltele Plateau (e.g., Corti et al., 2019). Eruptive centres dated at 1.9–0.3 Ma (Shinjo et al., 2011) lie along the margins of the Ririba fault zone; the youngest flows are not cut by faults. The Ririba rift experienced a few earthquakes that occurred along a projection of an east-dipping fault.

4.1.3 | Turkana Depression – ER linkage (Profile C-C′)

South of 4°N the rift zone is characterized by sub-parallel fault bounded basins that show a progressive west to east age progression, but most of the seismicity is concentrated across the lowest elevation region partially filled by Lake Turkana (Figures 5 and 6).

4.1.3.1 | *Turkwel basin*

The approximately N–S striking Turkwel escarpment marks the western margin of the Turkana Depression. Structures in the Turkwel basin strike N-S, with no intrabasinal faults evident at the surface. The basin is ca. 100 km long and ca. 40 km wide, but no subsurface data exist.

4.1.3.2 | *Lokichar basin*

The ca. 25 km-wide Lokichar half-graben parallels the Turkwel escarpment, and it is bounded on its western side by a N-S-striking border fault. The westward-tilted Lokichar basin has a basin infill thickness of ca. 4 km based on interpretation of seismic reflection calibrated by well data that did not reach crystalline basement (Schofield et al., 2021). Well data indicate the basin existed by Oligocene time, and a thick sequence of volcanic and clastic Miocene strata is overlain by a thin Pliocene-Recent sequence (Schofield et al., 2021). The Lokichar basin has moderate seismicity, and it was also the site of fluid injection for oil production in 2019–2020. A single focal mechanism (event 21, Figure 6) indicates oblique compression along NE-striking planes. Crust thins to 26 km beneath the basin (Figure 7; Ogden et al., 2023), with the maximum thinning along a projection of the border fault to the base of the crust, rather than the offset to the east offset predicted by a shallow detachment fault (Morley et al., 1999).

4.1.3.3 | *Kerio basin*

East of the Lokichar basin is the 60-km-long, 40-km-wide Kerio basin bounded on its western side by the Kerio border fault (Figures 5–7). Sediment thickness is ca. 4 km, but the thickest sequence is Pliocene-Recent, in contrast to the Oligo-Miocene dominated Lokichar basin to the west (Schofield et al., 2021). Stratal rotations along intrabasinal normal faults expose Middle-Miocene basaltic rocks at the surface (Figure 7).

4.1.3.4 | *Central Turkana Basin*

This ca. 60 km-wide basin, ca. 70 km-long basin is marked by low relief border faults on both its western and eastern sides. Crustal thickness is about 20 km based on refraction imaging (Mechie et al., 1994). Legacy seismic data indicate stratal thicknesses of ca. 3 km, but basement was not clearly imaged (Dunkleman et al., 1989). Neither the western nor the eastern border faults were seismically active during the 2-year TRAILS observation period. Instead, seismicity was focused along a persistent pipelike cluster between North Island and Central Island volcanoes that spans 20 km to surface near volcanic intrusions imaged in seismic reflection data (Dunkleman et al., 1989), suggesting magma and volatile release. Clusters of earthquakes at the southern end of the Central basin lie along projections of approximately N–S striking normal faults: events 9, 12, 13, 27, 28, and 40 indicate slip along NNW to NNE-striking nodal planes (Figure 6). The M_L 2.0 event 30 indicates extension along NNW-striking planes. Events 5 and 30 indicate oblique slip along NNE-striking nodal planes.

4.1.3.5 | *South Turkana basin*

The South Turkana basin is a narrow segment bounded on both sides by N-S striking normal faults, and with crustal thickness of ca. 20 km (Mechie et al., 1994; Ogden et al., 2023; Figures 5–7). Faults bounding the eastern side of the South Basin offset 3.0–2.2 Ma lavas of Longipi and Kulal shield volcanoes (Bruhn et al., 2011). This short rift segment includes South Island volcano near its centre, and it links the Turkana rift to the narrow Suguta rift, the active rift zone within the broader Miocene-Recent ER. Fault orientations in this rift sector range from N0°-10°. Seismicity occurs from the surface to about 15 km along closely-spaced N10-20E-striking faults beneath the western side of the basin. Strike-slip events 10, and 58 and reverse fault event 25 occurred near the tips of faults imaged in reflection seismic data (Muirhead et al., 2022). South Island volcano

is seismically inactive, arguing against a pressurized magma chamber.

4.1.3.6 | *Eliye Kink*

Central basin and South basin segments are linked via the Eliye kink, which is dominated by en echelon normal faults with relay ramps between left-stepping en echelon normal faults (and potentially dikes). The Eliye kink hosted event 49, the Mw 5 (M_L 4.5) May 3, 2020 earthquake with a N-S striking normal fault mechanism (Figure 6). Normal faulting events 9, 20, 40, 49, and 51 at 5–22 km depth have nodal planes steeper than 45°, as in basins to the north. Oblique-slip events 33 and 42 show extension along NE-striking nodal planes, whereas and Events 25 and 58 show left-lateral slip along sub E-W striking nodal planes.

4.1.3.7 | *Kino Sogo rift*

The Kino Sogo fault zone lies along the eastern flank of Lake Turkana and south of the Chew Bahir basin. Small offset faults and monoclines of the Kino Sogo fault belt developed concurrent with or after fissural eruptions at 4.05–3.95 Ma when the Gombe group basalts erupted and flowed eastwards into the Anza depression (Bruhn et al., 2011). Palaeomagnetic data indicate that the Gombe sequence was erupted earlier, and over the shorter time interval of 4.29–4.18 Ma (Erbello & Kidane, 2018). Monogenetic cones in the southern Chew Bahir basin mark the northern tip of this fault zone (Bruhn et al., 2011; Ebinger et al., 2000). Although it appears as a potential connection between Chew Bahir and the South Turkana basin, it is seismically inactive, as suggested from morphological analyses (Corti et al., 2019), and geodetic data (Musila et al., 2023). We find structures or seismicity supporting the NE-striking lineaments inferred by Vétel and Le Gall (2006).

4.1.3.8 | *Anza rift and <3 Ma eruptive centres*

Faults bounding the Mesozoic Anza Graben and the South Sudan rift are not readily evident in surface topography, but Bouguer gravity data calibrated by well and seismic data indicate that the basin is bounded by NW-SE striking border faults (Dindi, 1994; Figures 6 and 7). The low relief of the Anza rift east of Lake Turkana is interrupted by elongate shield volcanoes with NNE to NE-trending chains of eruptive centres and maars: Hurri Hills, Marsabit, Kulal, and Longipi. Hurri Hills and Marsabit have parasitic cones aligned along NNE-striking trends (e.g., Mazzarini & Isola, 2022), but there is no apparent elongation of calderas indicating extension (Franceschini et al., 2020). An enigma is the NW-striking Mega escarpment which parallels the Anza graben border faults (Figure 5). The parallelism of the Mega escarpment with the Mesozoic Anza bounding fault suggests that it may be an erosional remnant of the original uplifted flank to the Anza rift.

4.1.3.9 | *Eastern rift*

At the southern end of the study area, strain and magmatism within the initially ca. 60 km-wide S. Kerio basin migrated eastwards from near the Tanzania craton boundary to the ca. 20 km-wide Suguta rift (e.g., Baker, 1986; Bosworth & Maurin, 1993; Figure 5). Although the Chew Bahir-Kino Sogo Fault Belt rift zone marks the shortest linkage between the MER and the Suguta rift, the Lake Turkana rift zone ca. 50 km to the west is the current locus of strain (Figure 5).

Summarizing, the highest density of earthquakes occurs in the Eliye and Weyto kink zones rather than along border fault systems, although focal mechanisms are still predominantly classified as normal in these rift offset zones. Earthquakes occur in areas with and without magmatism, as illustrated in the three cross sections (Figure 7). Earthquakes occur throughout the crust, primarily along projections of border faults along planes dipping ≥45°, arguing against low-angle faults detaching in the mid-crust (e.g., Morley et al., 1999, 2020; Muirhead et al., 2022; Vétel & Le Gall, 2006).

4.2 | Border faults and extension direction

Most focal mechanisms of local and teleseismically detected earthquakes show normal faulting along N-S striking planes, and oblique-slip motion along NE and NW-striking nodal planes (Figures 3 and 6). There is a potential bias to strike-slip faults at the northern and southern edges of our array owing to azimuthal gaps that prevent resolution of approximately N–S striking nodal planes (e.g., Musila et al., 2023). Considering that the teleseisms release one to four orders of magnitude more energy than the local earthquakes, they provide key information on the regional opening direction.

We used the stress inversion method of Martínez-Garzón et al. (2014) to determine σ_1, σ_2, σ_3 and their uncertainties using 200 random bootstrap resampling of input focal mechanism solutions in the Eliye kink area (Figure 8), and we adopt the opening directions for the BRZ and Turkana rift from Musila et al. (2023). The best-fitting opening direction is N82E +20/−24° and identical, within uncertainties, of the geodetically determined Turkana rift opening direction of N88E (orange arrow; Musila et al., 2023). The smearing of σ_2 is expected with both left lateral and right lateral slip planes in these closely spaced extensional fault arrays.

4.3 | Kinematic Models

The diachronous cooling histories inferred from thermochronology in the BRZ all suggest that linkage between the MER and ER has changed with time since the MER initiated by about 12 Ma (e.g., Erbello et al., 2024). Considering the west to east migration across the Turkana depression to the current locus beneath Lake Turkana and the Ririba rift failure, we infer that the present linkage geometry has developed over the past 2.5 My (e.g., Corti et al., 2019; Schofield et al., 2021). We use rigid block models to evaluate current rift linkage, and evaluate models with comparison to the 16 GNSS measurements in Figures 4 and 9, as well as regional data. We assume that the area west of the BRZ is part of the stable Nubian plate. GNSS stations XLOK, LOCH, and KAKE show no significant motion relative to stable Nubia, so any linkage must lie north of ca. 5 N (Figure 9).

In our block modelling, Model 1 and Model 2 test differing orientations of the modern plate boundary(ies) between the MER and ER. These models include either a simplification of the BRZ between the MER and ER as a single boundary following Musila et al. (2023), or a boundary along a reactivated northern boundary of the Anza rift, respectively. In these two models, the main boundary follows the western escarpment of both the MER and the ER. In Model 3, we implement a third block that encompasses the BRZ as an individual block bounded by the Omo and North Omo basins to the West and extending to the Segen Basin in the East. Model 4 enlarges the third block by moving its boundary to the northern edge of the Anza rift zone. Additionally, as regional rates of deformation are relatively low, the influence of fault locking on model outputs is expected to be small. While we have drawn these boundaries, it is also important to note that all evidence indicates a broad region of deformation accommodates the modern linkage between the MER and ER. Our simplified modelling, therefore, is meant primarily to probe the large-scale kinematics and is not representative of the complexities of the entire system, tests of which would require denser geodetic arrays.

Results of this modelling are summarized in Table 1. Overall, the lowest RMS value is that from Model 4, which represents the BRZ as its own block, or microplate. Among the single boundary models, Model 1, which approximates the linkage between the MER and ER as a free slip boundary across the BRZ yields low RMS values. By contrast Model 2, which approximates this linkage as a reactivated Mesozoic fault on the northern edge of the Anza graben, does not yield as low RMS values. In comparing our models using the AIC and AIC_c, we find that Model 1 yields the lowest values, indicating that it represents the best balance between fit and increasingly complex models. However, additional velocity measurements could change this result.

5 | DISCUSSION

Our new results and existing data constrain the kinematics of modern rift sector linkage between the southern MER and the ER.

5.1 | Border fault geometries and extension direction

Earthquakes span the surface to 20 km depth throughout the study region, including beneath the Turkana basins where crustal thickness is ca. 20 km (Figure 7). Most earthquakes, and the largest magnitude earthquakes, occur along projections of border and transfer faults to lower crustal depths, arguing against a weak lower crust and detachment faults soling at depths <10 km (Boone, Balestrieri, et al., 2019; Morley et al., 1999). For example, the full moment tensor inversion for the M_L 4.5 May 3, 2019 earthquake has nodal planes dipping at ca. 45° at a rupture depth of 10 km (Musila et al., 2023; Figure 7c). Although we cannot accurately relocate the teleseismically detected earthquakes with nodal planes dipping ca. 45°, comparison with local seismicity suggests that they occurred along the border faults.

The ca. 35° change in seismically and geodetically determined extension direction from approximately N90°E across the ER and Turkana rift to N125°E across the MER occurs across the BRZ (Knappe et al., 2019; Musila et al., 2023; Figure 4). The exceptions are GNSS data from the western BRZ that indicate a local rotation in extension direction to N50-70E (Figure 4). Although GNSS data from South Sudan are needed to evaluate block Model 4, consideration of the BRZ as a distinct block with a speculative western boundary reproduces GNSS data, within uncertainties, suggesting counterclockwise rotations about vertical axes along NE- and NW-striking faults (Figure 9d). Philippon et al. (2014) also suggested a CCW rotation of extension direction in the western BRZ based on analogue modelling.

5.2 | Pre-existing structures and heterogeneities

Our work and earlier studies find little evidence for reactivation of Mesozoic Anza rift border and intrabasinal faults (e.g., Morley et al., 1992). Instead, the Oligocene-Recent

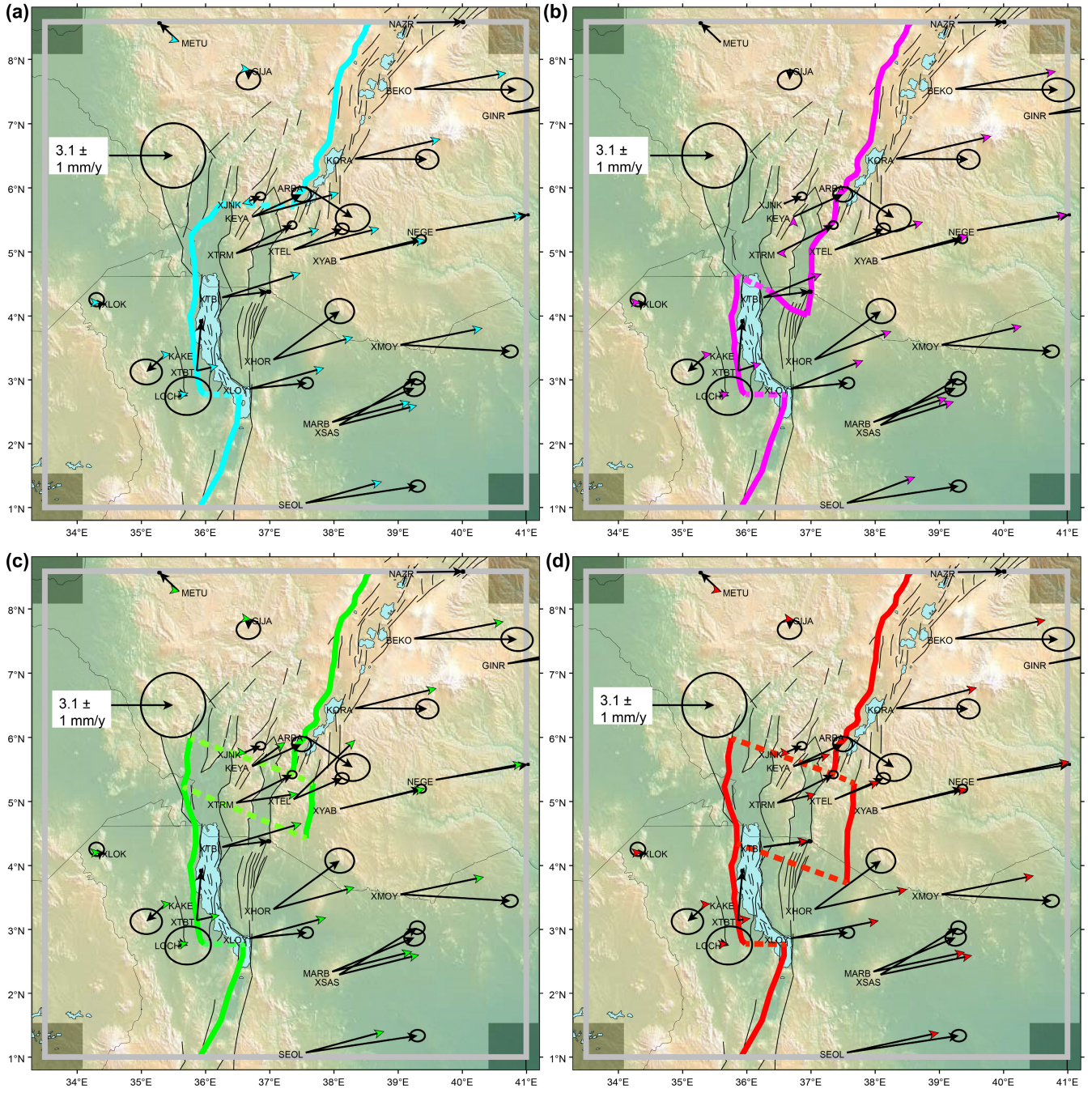

FIGURE 9 Maps showing different block model configurations and their model output. In all panels, black arrows indicate observed GNSS velocities, while the coloured arrows represent TDEFNODE-derived block motion. Pseudofaults are coloured grey while input faults and TDEFNODE-derived block motion at all stations are coloured according to Table 1. (a) Model 1 with faults and predicted velocity arrowheads in cyan. (b) Model 2 with faults and predicted velocities in magenta. (c) Model 3 with faults and predicted velocities in green. (d) Model 4 with faults and predicted velocities in red.

rift boundary appears to circumnavigate the Mesozoic Anza graben, which may have been stronger than surrounding crust at rift onset in Oligocene time, owing to the larger ratio of strong lithospheric mantle to weak crust (Ogden et al., 2023). The Mega escarpment is sub-parallel to, but lies ca. 25 km north of, the Anza border fault; it may represent an erosional remnant of the former uplifted flank to the Anza rift (e.g., Sacek, 2017).

Although short segments of basin-bounding faults strike both NW and NE parallel to basement strain fabrics in the BRZ, the orientations of border fault systems across the BRZ and the Turkana Depression are approximately perpendicular to the regional, active extension directions determined from earthquake source mechanisms and from GNSS velocity vectors (Knappe et al., 2019; Musila et al., 2023; Figures 3–6). For

TABLE 1 Summary of block modelling results. AIC is the least squares case of the Akaike information criterion (AIC), and AIC_c is its sparse observation equivalent.

Model	Residual RMS	# blocks	Degrees of freedom	# obs	AIC	ΔAIC	AIC_c	ΔAIC_c	Colour
1	1.240	2	8	22	20.737	0.000	31.814	0.000	Cyan
2	1.422	2	8	22	23.740	3.003	34.816	3.003	Magenta
3	1.185	3	12	22	27.735	6.998	62.402	30.588	Green
4	1.075	3	12	22	25.582	4.845	60.249	28.435	Red

example, along the southwestern side of the Chew Bahir basin, or the Aluma basin, short NW-striking faults parallel basement shear zones and link NNE-striking segments (Figures 5 and 6). Other NNW-trending segments in SW Ethiopia parallel the axes of Pan-African syn-forms and anti-forms, but cross-cut shallow dipping fabrics on fold limbs (Davidson & Shiferaw, 1983; Ebinger et al., 2000; Erbello et al., 2022, 2024; Philippon et al., 2014). Fault arrays that form early in rift history may be non-optimally orientated structures that reactivate basement fabric, such as the zig-zag patterns in the BRZ (e.g., Cowie et al., 2000; Nutz et al., 2022). In other areas, border faults cross-cut the NW-striking shear zones bounding accreted terranes, as mapped by Davidson and Shiferaw (1983) and Erbello et al. (2022, 2024), again suggesting that reactivation is local.

Pre-existing lithospheric heterogeneities may play a role in the distinct broadening of the active rift zone into the ca. 250 km-wide, seismically active BRZ where extension direction rotates counterclockwise from ENE across the BRZ and southern MER to approximately E–W across the Turkana rift (Figures 3 and 9). The BRZ transects a NW-trending belt of ultra-mafic rocks underlain by high velocity mantle lithosphere interpreted as a NW-trending island arc accreted during the Pan-African (Kounoudis et al., 2021, 2023). Dehydration reactions during mantle melting may have led to a more refractory mantle beneath the former Eo-Oligocene flood basalt province and explain the very small volume of Miocene-Recent magmatism across the BRZ (e.g., Kounoudis et al., 2023; Steiner et al., 2022). More localized crustal magma chambers and dikes of the flood magmatism episode may have created crustal compositional heterogeneities (Steiner et al., 2022) exploited in ca. 20 Ma-Recent rifting.

5.3 | Kinematics of rift linkage

The kinematics of rift linkage has changed with time as magmatism and faulting have migrated eastwards from the edge of the Tanzania craton to the Mesozoic Anza rift over the past ca. 27 My, and strain is localized along the length of Lake Turkana, the current locus of subsidence (Knappe et al., 2019; Muirhead et al., 2022; Musila et al., 2023). The eastward migration of strain and magmatism associated with mantle dynamics has caused time-variations in linkage patterns; the current configuration probably developed in the past ca. 2.5 My.

Vétel and Le Gall (2006) interpret the right stepping, or eastward shifts in the rift axis as evidence for NE-striking shear zones. Fault kinematic data and existing data instead indicate that the diachroneity of ER and Turkana rift extension and eastward migration of magmatism led to the offset, or kink in the shape of the southern Turkana rift: the Eliye kink (Figure 8). As magmatic plumbing systems reached shallow crustal levels in the ER, strain localized to the central rift punctuated by eruptive centres during the past ca. 4 My. At ca. 4 Ma, Lake Turkana filled the Depression west of South Island volcano (Bruhn et al., 2011). Northward propagation of faulting and magmatism in the ER created a ca. 35 km-wide depression east of the former lake basin, and flank uplift effectively restructured the lake system, leading to an eastward shift in the depocentre (e.g., Bruhn et al., 2011; Schofield et al., 2021; Muirhead et al., 2022). The Eliye kink, therefore, achieves linkage of fault systems bounding Lake Turkana with the ER with no significant rotation in extension direction across the Eliye kink (Figure 8). The nodal planes of earthquakes at depths <15 km across the left-stepping Eliye kink and relay ramps indicate that linkage is accommodated by short, left-lateral, sub-E-W striking transfer faults (Figures 7 and 9).

The right-stepping BRZ is seismically and volcanically active across a ca. 250 km wide zone, effectively connecting the widely separated ER and MER. Many of the microseisms ($M_L \leq 2.5$) in the BRZ show oblique-slip along NE- to NNE-striking planes, suggesting that these short faults serve as dextral transfer zones achieving linkage of the broad zone of sub-parallel, weakly extended fault arrays between the MER and ER. The BRZ may have broadened as the Ririba rift developed over the past ca. 3.7 Ma (Corti et al., 2019; Erbello et al., 2022; Franceschini et al., 2020). The lack of seismicity in the Ririba rift suggests that the rift has failed, perhaps owing to the thinner and hence stronger crust of the Anza rift zone (e.g., Ogden et al., 2023), or abandonment as proposed by Corti et al. (2019).

The BRZ spans a NW-trending zone, or ribbon, of fast wavespeed mantle and crust intruded by flood magmatism that may be a distinct tectonic block with CCW rotations, as seen in Model 4 (Figure 9). Although a strong lithosphere would be expected to lead to more localized deformation, the ribbon of high-velocity mantle is narrow and may instead lead to diffuse extension on either side of the lateral mantle heterogeneity (e.g., England, 1983; Wenker & Beaumont, 2018), explaining the BRZ's unusual breadth. Fault systems form a splay pattern at the terrane boundary edges, producing a range of NW- to NE-striking fault planes and transfer fault zones, as shown in the simplified tectonic cartoon (Figures 5 and 10).

Earthquakes of M_L <2.5 corresponding to short faults have oblique-slip and strike-slip mechanisms at the tips of extensional fault arrays, creating a broad transtensional shear zone that effectively links disconnected border faults characterized by relay ramps at the surface (Figures 9 and 10). These short oblique-slip and strike-slip faults with both right lateral and left lateral slip link a wide array of active faults. Extension in the BRZ kink, therefore, can be explained by rift-perpendicular shearing at or near the tips of extensional faults arranged in a right-stepping en echelon pattern. A left-stepping pattern of dikes and normal faults linked by approximately E–W oblique-slip and strike-slip faults accommodates a more than 50 km eastward stepover of the Turkana rift to achieve linkage with the northernmost ER sector. This style of rift sector linkage is also seen in the zone of linkage between the southern Red Sea and Gulf of Aden rifts in the Afar depression where rift-perpendicular shearing achieves plate boundary linkage without the formation of through-going fault systems (Pagli et al., 2019).

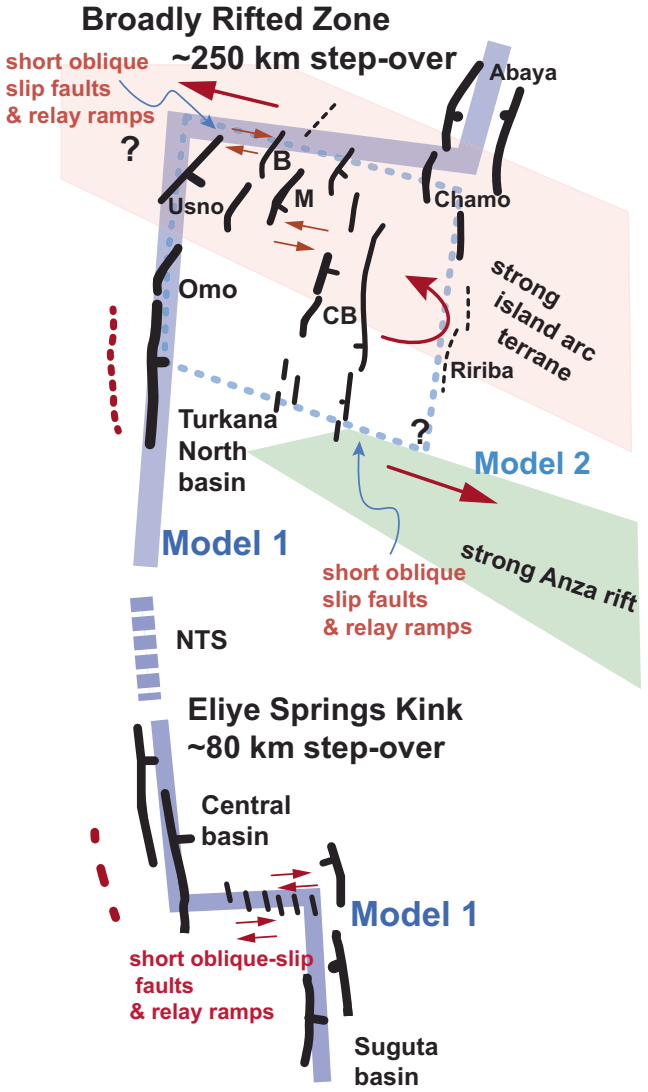

FIGURE 10 Models for rift linkage across the ca. 250 km-wide Broadly Rifted Zone (top right) and the Eliye Springs kink (bottom right). Strike-slip motion is achieved by short fault segments linking extensional fault arrays and no crustal-scale transform fault is formed. The Eliye kink developed in the past 2–4 My, whereas the BRZ is long-lived, in part explaining the locally varying GNSS opening vectors, and evidence for counterclockwise rotations about vertical axes.

6 | CONCLUSIONS

Our new syntheses of seismic, geodetic, stratigraphic, structural, and volcanological data from the zone of linkage between the southern MER and the ER through the Turkana Depression offer new constraints into the geometry and kinematics of rift zone linkage, and insights into rift zone evolution in heterogeneous continental lithosphere. Brittle strain across the ca. 250 km wide zone of right-stepping sub-parallel fault zones connecting the MER to the ER through the Turkana Depression is accommodated by steep normal faults linked with en echelon relay ramps and short oblique slip faults, rather than by through-going transform faults. Short segments of NE-striking basement structures facilitate across-rift linkage of faults, but NW-striking Mesozoic rift faults are not actively slipping, based on GNSS and seismicity data. Instead, the stronger (higher mantle: crust ratio) may have deflected rifting. Eastward migration of faulting and magmatism in the Turkana Depression, along-axis evolution of both the MER and ER, and lateral variations in crust and mantle structure all contributed to the unusual breadth of the zone of linkage between the MER and ER across the Turkana Depression.

Earthquake source mechanisms, block models of GNSS opening vectors, and structural data provide insights into the kinematics of rift sector linkage in response to lateral migration and along-axis propagation. The BRZ transecting an accreted terrane may be a discrete block with small

counterclockwise rotation that serves to connect the MER and ER. Strain across the BRZ and the Eliye kink is accommodated by en echelon normal faults linked by short strike-slip faults in crystalline basement, and relay ramps at the surface (Figure 10). Short segments of obliquely oriented basement structures facilitate across-rift linkage of faults, but basement shear zones and Mesozoic rift faults are not actively straining.

ACKNOWLEDGEMENTS

We thank Asfaw Erbello, M. Philippon, L. Pichel, and an anonymous reviewer for constructive and thoughtful feedback. We acknowledge the collaborative efforts of the University of Nairobi, Dedan Kimathi University and Addis Ababa University in all aspects of the Turkana Rift Array to Investigate Lithospheric Structure (TRAILS) network. Graduate students were instrumental in data acquisition in harsh field conditions: E. Knappe, S. Mwangi, M. Karanja, M. Wanyaga, B. Onguso, B. Kibret, and S. Alemayehu for assisting in the installation and servicing of the TRAILS seismic and geodetic networks. Sullivan digitized faults from field and high resolution imagery and collated existing data; Sullivan, Ebinger, Musila, Bastow, Perry collected and analysed the seismic and geodetic data; Kraus analysed source mechanisms; Sullivan, Kraus, Musila, Ebinger, Perry made figures; Sullivan, Ebinger, Perry wrote the text; Perry conducted fault kinematic modelling; Bastow, Bendick and Ebinger conceived and funded the project. GS, CJE, MM acknowledge support from the National Science Foundation grant numbers 1824199, 1824417, and 1551823. I. Bastow acknowledges support from Natural Environment Research Council grant number NE/S014136/1. For the purpose of open access, the author has applied a Creative Commons Attribution (CC BY) licence to any Author Accepted Manuscript (AAM) version arising.

PEER REVIEW

The peer review history for this article is available at https://www.webofscience.com/api/gateway/wos/peer-review/10.1111/bre.12900.

DATA AVAILABILITY STATEMENT

Seismic data obtained from the TRAILS project are archived at IRIS under two network codes Y1 (Ebinger, 2018) and 6R (Bastow, 2019). Data from an additional permanent seismic station, LODK, were sourced from OREFUS (https://www.orfeus-eu.org). The earthquake catalogue is archived with Musila et al. (2023). In the southern MER, we used seismic data from temporary seismic station, ARGA, as part of the Lake Abaya project (Ogden et al., 2021). Campaign and continuous geodetic data are archived at UNAVCO (Bendick, 2007, 2013). Digital fault arrays are provided as supplementary material. Digital fault data are available in the Supplementary materials.

ORCID

C. J. Ebinger https://orcid.org/0000-0002-6211-3399
M. Musila https://orcid.org/0000-0002-4865-6493
Mason Perry https://orcid.org/0000-0003-1719-9004
Ian Bastow https://orcid.org/0000-0003-1468-9278
Becks Bendick https://orcid.org/0000-0003-4204-3546

REFERENCES

Abdelfettah, Y., Tiercelin, J. J., Tarits, P., Hautot, S., Maia, M., & Thuo, P. (2016). Subsurface structure and stratigraphy of the northwest end of the Turkana Basin, Northern Kenya Rift, as revealed by magnetotellurics and gravity joint inversion. *Journal of African Earth Sciences*, *119*, 120–138.

Abdelsalam, M. G., & Stern, R. J. (1996). Sutures and shear zones in the Arabian-Nubian Shield. *Journal of African Earth Sciences*, *23*(3), 289–310.

Akaike, H. (1974). A new look at the statistical model identification. *IEEE Transactions on Automatic Control*, *19*(6), 716–723. https://doi.org/10.1109/TAC.1974.1100705

Alemu, T. (2017). Seismic reflection studies of South Omo Basin, Southwestern Ethiopia. Master Thesis, Addis Ababa University, 63 pp. http://213.55.95.56/handle/123456789/7766

Asfaw, L. M. (1990). Implication of shear deformation and earthquake distribution in the East African Rift between 4 N and 6 N. *Journal of African Earth Sciences (and the Middle East)*, *10*(4), 745–751.

Ayalew, D., Getaneh, W., Pik, R., Atnafu, B., Zemelak, A., & Belay, E. (2021). Stratigraphic framework of the northeastern part of the Ethiopian flood basalt province. *Bulletin of Volcanology*, *83*, 1–13.

Baker, B. H. (1986). Tectonics and volcanism of the southern Kenya Rift Valley and its influence on rift sedimentation. *Geological Society, London, Special Publications*, *25*(1), 45–57.

Balestrieri, M. L., Bonini, M., Corti, G., Sani, F., & Philippon, M. (2016). A refinement of the chronology of rift-related faulting in the broadly rifted zone, Southern Ethiopia, through apatite fission-track analysis. *Tectonophysics*, *671*, 42–55.

Bastow, I. (2019). Turkana Rift arrays to investigate lithospheric strains—UK component [Dataset]. International Federation of Digital Seismograph Networks https://doi.org/10.7914/SN/6R_2019

Bendick, R., & Reilinger, R. E. (2007). Ethiopia 2007, GAGE facility, GPS/GNSS observations Dataset. https://doi.org/10.7283/T5T43R0W

Bendick, R., & Knappe, E. (2013). Ethiopia Tectonics GPS Network – BDMT-Bahir Dar P.S., GAGE facility, GPS/GNSS observations Dataset. https://doi.org/10.7283/T52R3PMH

Bialas, R. W., Buck, W. R., & Qin, R. (2010). How much magma is required to rift a continent? *Earth and Planetary Science Letters*, *292*(1–2), 68–78.

Birhanu, Y., Bendick, R., Fisseha, S., Lewi, E., Floyd, M., King, R., & Reilinger, R. (2016). GPS constraints on broad scale extension in the Ethiopian Highlands and Main Ethiopian Rift. *Geophysical Research Letters*, *43*(13), 6844–6851.

Boniface, N., & Appel, P. (2018). Neoproterozoic reworking of the Ubendian Belt crust: Implication for an orogenic cycle between the Tanzania Craton and Bangweulu Block during the assembly of Gondwana. *Precambrian Research*, *305*, 358–385.

Boone, S. C., Balestrieri, M. L., Kohn, B. P., Corti, G., Gleadow, A. J. W., & Seiler, C. (2019). Tectonothermal evolution of the broadly rifted zone, Ethiopian Rift. *Tectonics*, *38*(3), 1070–1100.

Bosworth, W., & Maurin, A. (1993). Structure, geochronology and tectonic significance of the northern Suguta Valley (Gregory Rift), Kenya. *Journal of the Geological Society*, *150*(4), 751–762.

Bosworth, W., & Morley, C. K. (1994). Structural and stratigraphic evolution of the Anza rift, Kenya. *Tectonophysics*, *236*, 93–115.

Boyce, A., Kounoudis, R., Bastow, I., Cottaar, S., Ebinger, C., & Ogden, C. (2023). Mantle wavespeed and discontinuity structure below East Africa: Implications for Cenozoic hotspot tectonism and the development of the Turkana. *Depression*, *24*(8), e2022GC010775.

Bruhn, R. L., Brown, F. H., Gathogo, P. N., & Haileab, B. (2011). Pliocene volcano-tectonics and paleogeography of the Turkana Basin, Kenya and Ethiopia. *Journal of African Earth Sciences*, *59*(2–3), 295–312.

Brune, S., Corti, G., & Ranalli, G. (2017). Controls of inherited lithospheric heterogeneity on rift linkage: Numerical and analog models of interaction between the Kenyan and Ethiopian rifts across the Turkana depression. *Tectonics*, *36*(9), 1767–1786.

Brune, S., Kolawole, F., Olive, J. A., Stamps, D. S., Buck, W. R., Buiter, S. J., Furman, T., & Shillington, D. J. (2023). Geodynamics of continental rift initiation and evolution. *Nature Reviews Earth and Environment*, *4*(4), 235–253.

Brune, S., Williams, S. E., & Müller, R. D. (2018). Oblique rifting: The rule, not the exception. *Solid Earth*, *9*(5), 1187–1206.

Buck, W. R. (2004). Consequences of asthenospheric variability on continental rifting. In *Rheology and deformation of the lithosphere at continental margins* (pp. 1–30). Columbia University Press.

Burnham, K. P., & Anderson, D. R. (2002). *Model selection and multimodel inference: A practical information-theoretic approach* (2nd ed.). Springer. https://doi.org/10.1016/j.ecolmodel.2003.11.004

Burov, E. B., & Diament, M. (1995). The effective elastic thickness (T e) of continental lithosphere: What does it really mean? *Journal of Geophysical Research: Solid Earth*, *100*(B3), 3905–3927.

Chang, S.-J., Kendall, E., Davaille, A., & Ferreira, A. M. G. (2020). The evolution of mantle plumes in East Africa. *Journal of Geophysical Research*, *125*. https://doi.org/10.1029/2020jb019929

Chorowicz, J. (2005). The east African rift system. *Journal of African Earth Sciences*, *43*(1–3), 379–410.

Cinti, F. R., Pantosti, D., De Martini, P. M., Pucci, S., Civico, R., Pierdominici, S., Cucci, L., Brunori, C. A., Pinzi, S., & Patera, A. (2011). Evidence for surface faulting events along the Paganica fault prior to the 6 April 2009 L'Aquila earthquake (central Italy). *Journal of Geophysical Research*, *116*(B7).

Corti, G. (2009). Continental rift evolution: From rift initiation to incipient break-up in the Main Ethiopian Rift, East Africa. *Earth Science Reviews*, *96*(1–2), 1–53.

Corti, G., Cioni, R., Franceschini, Z., Sani, F., Scaillet, S., Molin, P., Isola, I., Mazzarini, F., Brune, S., Keir, D., & Erbello, A. (2019). Aborted propagation of the Ethiopian rift caused by linkage with the Kenyan rift. *Nature Communications*, *10*(1), 1309.

Cowie, P. A., Gupta, S., & Dawers, N. H. (2000). Implications of fault array evolution for synrift depocentre development: Insights from a numerical fault growth model. *Basin Research*, *12*(3–4), 241–261.

Craig, T. J., & Jackson, J. A. (2021). Variations in the seismogenic thickness of East Africa. *Journal of Geophysical Research: Solid Earth*, *126*(3), e2020JB020754.

Davidson, A., compiler. (1983). *Reconnaissance geology and geochemistry of parts of llubabor, Kefa, Gemo Gofa and Sidamo* (Ethiopian Institute of Geological Surveys, Bulletin No. 2), 89 p.

Davidson, A., & Rex, D. C. (1980). Age of volcanism and rifting in southwestern Ethiopia. *Nature*, *283*, 657–658.

Davidson, A., & Shiferaw, A. (1983). The Omo river project, reconnaissance geology and geochemistry of parts of Ilubabor, Kefa, Gemu Gofa and Sidamo, Ethiopia. *Ethiopian Institute of Geological Survey Bulletin*, *2*, 1–89.

Dindi, E. W. (1994). Crustal structure of the Anza graben from gravity and magnetic investigations. *Tectonophysics*, *236*(1–4), 359–371.

Dunkleman, T. J., Rosendahl, B. R., & Karson, J. A. (1989). Structure and stratigraphy of the Turkana Rift from seismic reflection data. *Journal of African Earth Sciences*, *8*(2-4), 489–510.

Dunkley, P. N., Smith, M., Allen, D. J., & Darling, W. G. (1993). The geothermal activity and geology of the northern sector of the Kenya Rift Valley. British Geological Survey. Research Report SC/93/1.

Dziewonski, A. M., Chou, T. A., & Woodhouse, J. H. (1981). Determination of earthquake source parameters from waveform data for studies of global and regional seismicity. *Journal of Geophysical Research: Solid Earth*, *86*, 2825–2852.

Ebinger, C., van Wijk, J., Olaka, L., Mériaux, C., & Fontijn, K. (2023). All scales must be considered to understand rifts. *Nature Reviews Earth and Environment*, *4*(4), 209–210.

Ebinger, C., Yemane, T., WoldeGabriel, G., Aronson, J., & Walter, R. (1993). Eocene-recent volcanism and faulting in the southern Main Ethiopian rift. *Journal of the Geological Society of London*, *150*(99–108), 108.

Ebinger, C. J. (2018). Crust and mantle structure and the expression of extension in the Turkana depression of Kenya and Ethiopia [data set]. *International Federation of Digital Seismograph Networks*. https://doi.org/10.7914/SN/Y1_2018

Ebinger, C. J., & Casey, M. (2001). Continental breakup in magmatic provinces: An Ethiopian example. *Geology*, *29*, 527–530.

Ebinger, C. J., Yemane, T., Harding, D., Tesfaye, S., Kelley, S., & Rex, D. C. (2000). Rift deflection, migration, and propagation: Linkage of the Ethiopian and Eastern rifts, Africa. *Geological Society of America Bulletin*, *112*(2), 163–176.

Ekström, G., Nettles, M., & Dziewoński, A. M. (2012). The global CMT project 2004–2010: Centroid-moment tensors for 13,017 earthquakes. *Physics of the Earth and Planetary Interiors*, *200*, 1–9.

England, P. (1983). Constraints on extension of continental lithosphere. *Journal of Geophysical Research: Solid Earth*, *88*(B2), 1145–1152.

Erbello, A., Colleps, C., Melnick, D., Sobel, E. R., Bookhagen, B., Pingel, H., Zeilinger, G., van der Beek, P., & Strecker, M. R. (2024). Magma-assisted continental rifting: The broadly rifted zone in SW Ethiopia, East Africa. *Tectonics*, *43*(1), e2022TC007651.

Erbello, A., & Kidane, T. (2018). Timing of volcanism and initiation of rifting in the Omo-Turkana depression, southwest Ethiopia:

Evidence from paleomagnetism. *Journal of African Earth Sciences*, *139*, 319–329.

Erbello, A., Melnick, D., Zeilinger, G., Bookhagen, B., Pingel, H., & Strecker, M. R. (2022). Geomorphic expression of a tectonically active rift-transfer zone in Southern Ethiopia. *Geomorphology*, *403*, 108162.

Fishwick, S., & Bastow, I. D. (2011). Towards a better understanding of African topography: A review of passive-source seismic studies of the African crust and upper mantle. *Geological Society, London, Special Publications*, *357*(1), 343–371.

Fossen, H., & Rotevatn, A. (2016). Fault linkage and relay structures in extensional settings—A review. *Earth-Science Reviews*, *154*, 14–28.

Foster, A. N., & Jackson, J. A. (1998). Source parameters of large African earthquakes: Implications for crustal rheology and regional kinematics. *Geophysical Journal International*, *134*(2), 422–448.

Franceschini, Z., Cioni, R., Scaillet, S., Corti, G., Sani, F., Isola, I., Mazzarini, F., Duval, F., Erbello, A., Muluneh, A., & Brune, S. (2020). Recent volcano-tectonic activity of the Ririba rift and the evolution of rifting in South Ethiopia. *Journal of Volcanology and Geothermal Research*, *403*, 106989.

Fritz, H., Abdelsalam, M., Ali, K. A., Bingen, B., Collins, A. S., Fowler, A. R., Ghebreab, W., Hauzenberger, C. A., Johnson, P. R., Kusky, T. M., Macey, P., Muhongo, S., Stern, R. J., & Viola, G. (2013). Orogen styles in the east African Orogen: A review of the Neoproterozoic to Cambrian tectonic evolution. *Journal of African Earth Sciences*, *86*, 65–106. https://doi.org/10.1016/j.jafrearsci.2013.06.004

George, R., Rogers, N., & Kelley, S. (1998). Earliest magmatism in Ethiopia: Evidence for two mantle plumes in one flood basalt province. *Geology*, *26*(10), 923–926.

Global Volcanism Program. (2023). [database] volcanoes of the world (v.5.1.5; 15 Dec 2023). In *Distributed by Smithsonian Institution*, compiled by Venzke, E. https://doi.org/10.5479/si.GVP.VOTW5-2023.5.1

Gupta, S., Cowie, P. A., Dawers, N. H., & Underhill, J. R. (1998). A mechanism to explain rift-basin subsidence and stratigraphic patterns through fault-array evolution. *Geology*, *26*(7), 595–598.

Hackman, B. D., Charsley, T. J., Key, R. M., & Wilkinson, A. F. (1990). The development of the east African rift system in north-central Kenya. *Tectonophysics*, *184*(2), 189–211.

Hayward, N. J., & Ebinger, C. J. (1996). Variations in the along-axis segmentation of the Afar rift system. *Tectonics*, *15*(2), 244–257.

Hendrie, D. B., Kusznir, N. J., Morley, C. K., & Ebinger, C. J. (1994). Cenozoic extension in northern Kenya: A quantitative model of rift basin development in the Turkana region. *Tectonophysics*, *236*(1–4), 409–438.

Jicha, B. R., & Brown, F. H. (2014). An age for the Korath range, Ethiopia and the viability of $^{40}Ar/^{39}Ar$ dating of kaersutite in late Pleistocene volcanics. *Quaternary Geochronology*, *21*, 53–57.

Katumwehe, A. B., Abdelsalam, M. G., Atekwana, E. A., & Laó-Dávila, D. A. (2016). Extent, kinematics and tectonic origin of the Precambrian Aswa shear zone in eastern Africa. *Gondwana Research*, *34*, 241–253.

Kebede, B., Mammo, T., Shawel, M., & Alemu, T. (2023). Integrated seismic stratigraphic and structural analysis of southern Main Ethiopian rift basin: Implications for hydrocarbon potential. *Acta Geophysica*, *72*, 597–617. https://doi.org/10.1007/s11600-023-01111-7

Keranen, K., Klemperer, S. L., Gloaguen, R., & EAGLE Working Group. (2004). Three-dimensional seismic imaging of a proto-ridge axis in the Main Ethiopian rift. *Geology*, *32*(11), 949–952.

Key, R. M., Rop, B. P., & Rundle, C. C. (1987). The development of the late Cenozoic alkali basaltic Marsabit shield volcano, northern Kenya. *Journal of African Earth Sciences*, *6*(4), 475–491.

Key, R. M., & Watkins, R. T. (1988). Geology of the Sabarei area: Degree sheets 3 and 4, with coloured 1: 250 000 geological map and results of geochemical exploration. Geological Survey Kenya.

Kinabo, B. D., Atekwana, E. A., Hogan, J. P., Modisi, M. P., Wheaton, D. D., & Kampunzu, A. B. (2007). Early structural development of the Okavango rift zone, NW Botswana. *Journal of African Earth Sciences*, *48*(2–3), 125–136.

Knappe, E., Bendick, R., Ebinger, C. J., Birhanu, Y., Lewi, E., Floyd, M., King, R., Mariita, N., Timtime, T., Bekele, B., Deresse, B., Musila, M., Kanoti, J., & Perry, M. (2019). Accommodation of east African rifting across the Turkana depression. *Journal of Geophysical Research*. https://doi.org/10.1029/2019JB018469

Kolawole, F., Phillips, T. B., Atekwana, E. A., & Jackson, C. A. L. (2021). Structural inheritance controls strain distribution during early continental rifting, Rukwa rift. *Frontiers in Earth Science*, *9*, 707869.

Koptev, A., Calais, E., Burov, E., Leroy, S., & Gerya, T. (2018). Along-axis variations of rift width in a coupled lithosphere-mantle system, application to East Africa. *Geophysical Research Letters*, *45*(11), 5362–5370.

Kounoudis, R., Bastow, I. D., Ebinger, C. J., Darbyshire, F., Ogden, C. S., Musila, M., Ugo, F., Ayele, A., Sullivan, G., Bendick, R., & Mariita, N. (2023). The development of rifting and magmatism in the multiply rifted Turkana depression, East Africa: Evidence from surface-wave analysis of crustal and uppermost mantle structure. *Earth and Planetary Science Letters*, *621*, 118386.

Kounoudis, R., Bastow, I. D., Ebinger, C. J., Ogden, C. S., Bendick, R., Ayele, A., Mariita, N., Kianji, G., Wigham, G., Musila, M., & Kibret, B. (2021). Body wave tomographic imaging of the Turkana depression: Implications for rift development and plume-lithosphere interactions. *Geochemistry, Geophysics, Geosystems*.

Mammo, T. (2012). Analysis of gravity field to reconstruct the structure of Omo basin in SW Ethiopia and implications for hydrocarbon potential. *Marine and Petroleum Geology*, *29*(1), 104–114.

Martínez-Garzón, P., Kwiatek, G., Ickrath, M., & Bohnhoff, M. (2014). MSATSI: A MATLAB package for stress inversion combining solid classic methodology, a new simplified user-handling, and a visualization tool. *Seismological Research Letters*, *85*(4), 896–904.

Mazzarini, F., & Isola, I. (2022). Quaternary off-rift volcanism along a section of the east African rift system (EARS), from the South Ethiopia to the south Kenya. *Italian Journal of Geosciences*, *141*(3), 334–347.

McCaffrey, R. (2009). Time-dependent inversion of three-component continuous GPS for steady and transient sources in northern Cascadia. *Geophysical Research Letters*, *36*, L07304. https://doi.org/10.1029/2008GL036784

McDougall, I. A. N., & Brown, F. H. (2009). Timing of volcanism and evolution of the northern Kenya rift. *Geological Magazine*, *146*(1), 34–47.

Mechie, J., Keller, G. R., Prodehl, C., Gaciri, S., Braile, L. W., Mooney, W. D., Gajewski, D., & Sandmeier, K. J. (1994). Crustal structure

beneath the Kenya rift from axial profile data. *Tectonophysics*, *236*(1–4), 179–200.

Moore, J. M., & Davidson, A. (1978). Rift structure in Southern Ethiopia. *Tectonophysics*, *46*(1–2), 159–173. https://doi.org/10.1016/0040-1951(78)90111-7

Morley, C. K. (2020). Early syn-rift igneous dike patterns, northern Kenya rift (Turkana, Kenya): Implications for local and regional stresses, tectonics, and magma-structure interactions. *Geosphere*, *16*(3), 890–918.

Morley, C. K., Wescott, W. A., Stone, D. M., Harper, R. M., & Wigger, S. T. (1992). Tectonic evolution of the northern Kenyan rift. *Journal of the Geological Society*, *149.3*, 333–348.

Morley, C. K., Wescott, W. A., Stone, D. M., Harper, R. M., Wigger, S. T., Day, R. A., & Karanja, F. M. (1999). Geology and geophysics of the Western Turkana basins, Kenya. In C. K. Morley (Ed.), *Geoscience of rift systems—Evolution of East Africa* (Vol. *44*, pp. 19–54). AAPG Studies in Geology.

Muirhead, J. D., Fischer, T. P., Oliva, S. J., Laizer, A., van Wijk, J., Currie, C. A., Lee, H., Judd, E. J., Kazimoto, E., Sano, Y., & Takahata, N. (2020). Displaced cratonic mantle concentrates deep carbon during continental rifting. *Nature*, *582*(7810), 67–72.

Muirhead, J. D., Scholz, C. A., & Rooney, O. T. (2022). Transition to magma-driven rifting in the South Turkana Basin, Kenya: Part 1. *Journal of the Geological Society*, *179*(6), jgs2021-159.

Musila, M., Ebinger, C. J., Bastow, I. D., Sullivan, G., Oliva, S. J., Knappe, E., Perry, M., Kounoudis, R., Ogden, C. S., Bendick, R., Mwangi, S., Mariita, N., Kianji, G., Klein, E., & Illsley-Kemp, F. (2023). Active deformation constraints on the Nubia-Somalia Plate Boundary through Heterogeneous Lithosphere of the Turkana Depression. *Geochemistry, Geophysics, Geosystems*, *24*, e2023GC010982.

Nakai, J. S., Sheehan, A. F., & Bilek, S. L. (2017). Seismicity of the rocky mountains and Rio Grande rift from the EarthScope transportable Array and CREST temporary seismic networks, 2008–2010. *Journal of Geophysical Research: Solid Earth*, *122*(3), 2173–2192.

Neves, S. P., Tommasi, A., Vauchez, A., Carrino, T. A., & Banerjee, S. (2021). The Borborema strike-slip shear zone system (NE Brazil): Large-scale intracontinental strain localization in a heterogeneous plate. *Lithosphere*, *2022*, 26. https://doi.org/10.2113/2021/6407232

Nutz, A., Ragon, T., & Schuster, M. (2022). Cenozoic tectono-sedimentary evolution of the northern Turkana depression (east African rift system) and its significance for continental rifts. *Earth and Planetary Science Letters*, *578*, 117285.

Ogden, C., Keir, D., Bastow, I., Ayele, A., Marcou, S., Woodward, A., Abera, B., & Gudbrandsson, S. (2021). Seismicity and crustal structure of the southern Main Ethiopian rift: New evidence from Lake Abaya. *Geochemistry, Geophysics, Geosystems*, *22*. https://doi.org/10.1029/2021GC009831

Ogden, C. S., Bastow, I. D., Ebinger, C., Ayele, A., Kounoudis, R., Musila, M., Bendick, R., Mariita, N., Kianji, G., Rooney, T. O., & Sullivan, G. (2023). The development of multiple phases of superposed rifting in the Turkana depression, East Africa: Evidence from receiver functions. *Earth and Planetary Science Letters*, *609*, 118088.

Oliva, S. J., Ebinger, C. J., Wauthier, C., Muirhead, J. D., Roecker, S. W., Rivalta, E., & Heimann, S. (2019). Insights into fault-magma interactions in an early-stage continental rift from source mechanisms and correlated volcano-tectonic earthquakes. *Geophysical Research Letters*, *46*(4), 2065–2074.

Olive, J. A., Malatesta, L. C., Behn, M. D., & Buck, W. R. (2022). Sensitivity of rift tectonics to global variability in the efficiency of river erosion. *Proceedings of the National Academy of Sciences of the United States of America*, *119*(13), e2115077119.

Owusu-Agyemang, P. C., Roberts, E. M., Downie, B., & Sertich, J. J. (2019). Sedimentary provenance and maximum depositional age analysis of the cretaceous? Lapur and Muruanachok sandstones (Turkana grits), Turkana Basin, Kenya. *Geological Magazine*, *156*(8), 1334–1356.

Pagli, C., Yun, S.-H., Ebinger, C. J., Keir, D., & Wang, H. (2019). The origin of strike-slip tectonics in continental rift zones. *Geology*, *47*, 31–34. https://doi.org/10.1130/G45345.1

Petit, C., Burov, E., & Tiberi, C. (2008). Strength of the lithosphere and strain localisation in the Baikal rift. *Earth and Planetary Science Letters*, *269*, 523–529.

Philippon, M., Corti, G., Sani, F., Bonini, M., Balestrieri, M. L., Molin, P., Willingshofer, E., Sokoutis, D., & Cloetingh, S. (2014). Evolution, distribution, and characteristics of rifting in Southern Ethiopia. *Tectonics*, *33*, 485–508.

Ragon, T., Nutz, A., Schuster, M., Ghienne, J. F., Ruffet, G., & Rubino, J. L. (2019). Evolution of the northern Turkana depression (east African rift system, Kenya) during the Cenozoic rifting: New insights from the Ekitale Basin (28-25.5 Ma). *Geological Journal*, *54*, 3468–3488.

Reiss, M. C., Muirhead, J. D., Laizer, A. S., Link, F., Kazimoto, E. O., Ebinger, C. J., & Rümpker, G. (2021). The impact of complex volcanic plumbing on the nature of seismicity in the developing magmatic natron rift, Tanzania. *Frontiers in Earth Science*, *8*, 609805.

Roberts, H. M., Ramsey, C. B., Chapot, M. S., Deino, A. L., Lane, C. S., Vidal, C., Asrat, A., Cohen, A., Foerster, V., Lamb, H. F., & Schäbitz, F. (2021). Using multiple chronometers to establish a long, directly-dated lacustrine record: Constraining >600,000 years of environmental change at chew Bahir, Ethiopia. *Quaternary Science Reviews*, *266*, 107025.

Sacek, V. (2017). Post-rift influence of small-scale convection on the landscape evolution at divergent continental margins. *Earth and Planetary Science Letters*, *459*, 48–57.

Schofield, N., Newton, R., Thackrey, S., Watson, D., Jolley, D., & Morley, C. (2021). Linking surface and subsurface volcanic stratigraphy in the Turkana depression of the east African rift system. *Journal of the Geological Society*, *178*(1), jgs2020-110.

Shinjo, R., Chekol, T., Meshesha, D., Itaya, T., & Tatsumi, Y. (2011). Geochemistry and geochronology of the mafic lavas from the southeastern Ethiopian rift (the east African rift system): Assessment of models on magma sources, plume–lithosphere interaction and plume evolution. *Contributions to Mineralogy and Petrology*, *162*, 209–230.

Smith, M., & Mosley, P. (1993). Crustal heterogeneity and basement influence on the development of the Kenya rift, East Africa. *Tectonics*, *12*(2), 591–606.

Stamps, D. S., Calais, E., Saria, E., Hartnady, C., Nocquet, J. M., Ebinger, C. J., & Fernandes, R. M. (2008). A kinematic model for the East African Rift. *Geophysical Research Letters*, *35*(5), L05304. https://doi.org/10.1029/2007GL032781

Steiner, R. A., Rooney, T. O., Girard, G., Rogers, N., Ebinger, C. J., Peterson, L., & Phillips, R. K. (2022). Initial Cenozoic magmatic activity in East Africa: New geochemical constraints on magma

distribution within the Eocene continental flood basalt province. *Geological Society of Publications*, *518*, 435–465.

Styron, R., & Pagani, M. (2020). The GEM global active faults database. *Earthquake Spectra*, *36*, 160–180. https://doi.org/10.1177/8755293020944182

Tiercelin, J. J., Potdevin, J. L., Thuo, P. K., Abdelfettah, Y., Schuster, M., Bourquin, S., Bellon, H., Clément, J. P., Guillou, H., Nalpas, T., & Ruffet, G. (2012). Stratigraphy, sedimentology and diagenetic evolution of the Lapur sandstone in northern Kenya: Implications for oil exploration of the Meso-Cenozoic Turkana depression. *Journal of African Earth Sciences*, *71-72*, 43–79.

Torres Acosta, V., Bande, A., Sobel, E. R., Parra, M., Schildgen, T. F., Stuart, F., & Strecker, M. R. (2015). Cenozoic extension in the Kenya rift from low-temperature thermochronology: Links to diachronous spatiotemporal evolution of rifting in East Africa. *Tectonics*, *34*(12), 2367–2386.

Van Wijk, J., Axen, G., & Abera, R. (2017). Initiation, evolution and extinction of pull-apart basins: Implications for opening of the Gulf of California. *Tectonophysics*, *719*, 37–50.

Vétel, W., & Le Gall, B. (2006). Dynamics of prolonged continental extension in magmatic rifts: The Turkana rift case study (North Kenya). *Geological Society, London, Special Publications*, *259*, 209–233.

Weinstein, A., Oliva, S. J., Ebinger, C. J., Roecker, S., Tiberi, C., Aman, M., Lambert, C., Witkin, E., Albaric, J., Gautier, S., & Peyrat, S. (2017). Fault-magma interactions during early continental rifting: Seismicity of the Magadi-Natron-Manyara basins, Africa. *Geochemistry, Geophysics, Geosystems*, *18*(10), 3662–3686.

Weissel, J. K., & Karner, G. D. (1989). Flexural uplift of rift flanks due to mechanical unloading of the lithosphere during extension. *Journal of Geophysical Research: Solid Earth*, *94*(B10), 13919–13950.

Wenker, S., & Beaumont, C. (2018). Effects of lateral strength contrasts and inherited heterogeneities on necking and rifting of continents. *Tectonophysics*, *746*, 46–63.

Wichura, H., Jacobs, L. L., Lin, A., Polcyn, M. J., Manthi, F. K., Winkler, D. A., Strecker, M. R., & Clemens, M. (2015). A 17-My-old whale constrains onset of uplift and climate change in east Africa. *Proceedings of the National Academy of Sciences of the United States of America*, *112*(13), 3910–3915.

Williams, J. N., Fagereng, Å., Wedmore, L. N., Biggs, J., Mdala, H., Mphepo, F., & Hodge, M. (2022). Low dissipation of earthquake energy where a fault follows pre-existing weaknesses: Field and microstructural observations of Malawi's Bilila-Mtakataka fault. *Geophysical Research Letters*, *49*(8), e2021GL095286.

Wilson, J. T. (1966). Did the Atlantic close and then Re-open? *Nature*, *211*(5050), 676–681.

Winn, R. D., Steinmetz, J. C., & Kerekgyarto, W. L. (1993). Stratigraphy and rifting history of the Mesozoic-Cenozoic Anza rift, Kenya. *AAPG Bulletin*, *77*(11), 1989–2005.

Woldegabriel, G., Aronson, J. L., & Walter, R. C. (1990). Geology, geochronology, and rift basin development in the central sector of the Main Ethiopia rift. *Geological Society of America Bulletin*, *102*, 439–458.

WoldeGabriel, G., Yemane, T., Suwa, G., White, T., & Asfaw, B. (1991). Age of volcanism and rifting in the Burji-Soyoma area, Amaro Horst, southern Main Ethiopian rift: Geo-and biochronologic data. *Journal of African Earth Sciences*, *13*(3–4), 437–447.

Zheng, W., Oliva, S. J., Ebinger, C., & Pritchard, M. E. (2020). Aseismic deformation during the 2014 Mw 5.2 Karonga earthquake, Malawi, from satellite interferometry and earthquake source mechanisms. *Geophysical Research Letters*, *47*(22), e2020GL090930.

SUPPORTING INFORMATION

Additional supporting information can be found online in the Supporting Information section at the end of this article.

How to cite this article: Sullivan, G., Ebinger, C. J., Musila, M., Perry, M., Kraus, E. R., Bastow, I., & Bendick, B. (2024). Kinematics of rift linkage between the Eastern and Ethiopian rifts in the Turkana Depression, Africa. *Basin Research*, *36*, e12900. https://doi.org/10.1111/bre.12900